Resolution Measurement of an Interpolating Pad Chamber in the 9 GeV/c π^- Beam at BNL

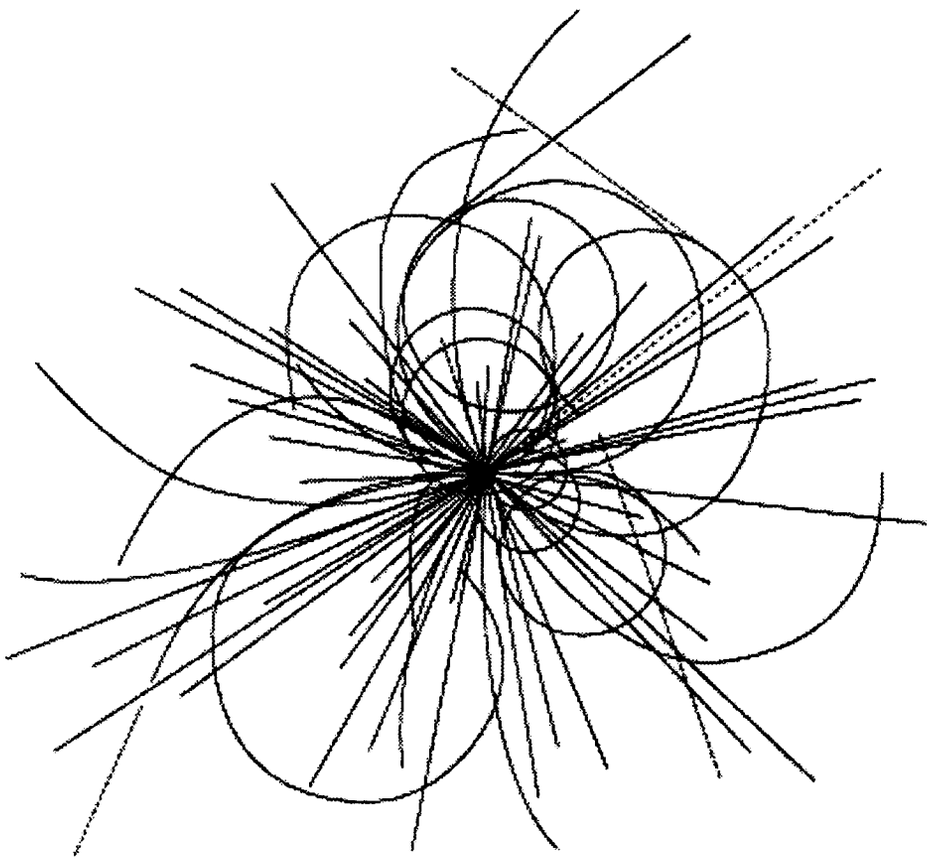

SSCL-Preprint-557
March 1994
Distribution Category: 414

H. Fenker
K. Morgan
R. Shypit
J. Thomas
C. Bower
J. Musser
M. Brooks
D. Lee
R. Martin
G. Mills
J. Romero
S. Alam
B. Nematti
J. O'Neill
H. Severini
C. Baltay
B. Barakat
W. Emmet
J. Sinnott
E. Wolin
G. Smith
B. Yu

Superconducting Super Collider Laboratory

SSCL-Preprint-557

Resolution Measurement of an Interpolating Pad Chamber in the 9 GeV/c π^- Beam at BNL*

H. Fenker, K. Morgan, R. Shypit, and J. Thomas

Superconducting Super Collider Laboratory†
2550 Beckleymeade Avenue
Dallas, Texas 75237

C. Bower and J. Musser

Indiana University
Bloomington, Indiana

M. Brooks, D. Lee, R. Martin, G. Mills, and J. Romero

Los Alamos National Laboratory
Los Alamos, New Mexico

S. Alam, B. Nematti, J. O'Neill, and H. Severini

SUNY at Albany
Albany, New York

C. Baltay, B. Barakat, W. Emmet, J. Sinnott, and E. Wolin

Yale University
New Haven, Connecticut

G. Smith and B. Yu

Brookhaven National Laboratory
Upton, New York

March 1994

* Accepted by *Nuclear Instruments and Methods.*
† Operated by the Universities Research Association, Inc., for the U.S. Department of Energy under Contract No. DE-AC35-89ER40486.

Resolution Measurement of an Interpolating Pad Chamber in the 9 GeV/c π^- Beam at BNL

H. Fenker, K. Morgan, R. Shypit, J. Thomas
SSC Laboratory, 2550 Beckleymeade Avenue, Dallas, Texas

C. R. Bower, J. Musser
Indiana University, Bloomington, Indiana

M. Brooks, D. Lee, R. Martin, G. Mills, J. Romero
Los Alamos National Laboratory, Los Alamos, New Mexico

S. Alam, B. Nematti, J. J. O'Neill, H. Severini
SUNY at Albany, Albany, New York

C. Baltay, B. Barakat, W. Emmet, J. Sinnott, E. Wolin
Yale University, New Haven, Connecticut

G. Smith, B. Yu
Brookhaven National Laboratory, Upton, New York

March 7, 1994

Abstract

Results are presented from the first test of a full size barrel prototype Interpolating Pad Chamber for the GEM central tracker in the 9 GeV/c π^- beam at the Brookhaven AGS. An average resolution of 45 μm has been achieved using electronics functionally identical to the final GEM design. Two 50 mRad stereo pad layers combine to give 680 μm resolution in the direction along the chamber. A calibration procedure which uses the data to measure the gains and pedestals for each pad has been developed and is presented together with resolution results from the silicon telescope used to project the tracks into the pad chambers.

1 Introduction

The resolution of a full size (200×25 cm^2) Interpolating Pad Chamber (IPC) for the GEM central tracker with 2.5 mm wide and 10 cm long pads was measured at the AGS at Brookhaven National Laboratory using 9 GeV/c pions and muons.

Until recently, Interpolating Pad Chambers have been used chiefly in fixed target experiments. They have been constructed with a massive frame, to ensure mechanical stability, kept outside the acceptance of the detector with no limit imposed on the thickness of the frame materials. In the case of IPCs constructed for the GEM central tracker, the frames cannot be placed outside the detector acceptance, and so a strong and stiff honeycomb core is utilized made from very light materials around which two chamber layers are constructed.

A track passing through the chamber gas deposits ionization which drifts towards the wire plane. The charge cluster on the wire induces a signal on the pad plane shared between the closest pads. The position is determined by interpolating between the three nearest pads using a parameterization of the electrostatics of the geometry. The pad chamber had two stereo pad planes allowing both a measurement in the transverse direction (x) as well as a measurement in the direction along the chamber (y) for tracks traversing both chambers. The z direction was defined as the direction along the beam. A silicon telescope was used to project the position of the tracks into the IPCs in both x and y. A schematic of the setup can be seen in Figure 1 and a cut away schematic of the chamber in Figure 2.

After alignment calibration of the detectors and determination of the gains and pedestals of the pad channels, the resolution of the pad planes was measured by taking the difference between the measured position in the pad chamber and the projected position from the silicon telescope. The x resolution was then studied as a function of a number of variables and is presented in Section 4. A study of the resolution using only two out of the three pads in the functional fit was also performed. This is of extreme importance for working situations where one electronics channel is not operational.

2 Experimental Apparatus

2.1 The Silicon Detectors

The silicon telescope was made with Micron OPAL-type [1] AC coupled silicon strip detectors. The strip pitch was 25 μm and every other strip was bonded to the readout electronics, giving a readout pitch of 50 μm. The dimensions of the detectors were 300 μm $\times$ 3.3 cm $\times$ 6.0 cm. The readout chips were CDF SVX-D [2] chips.

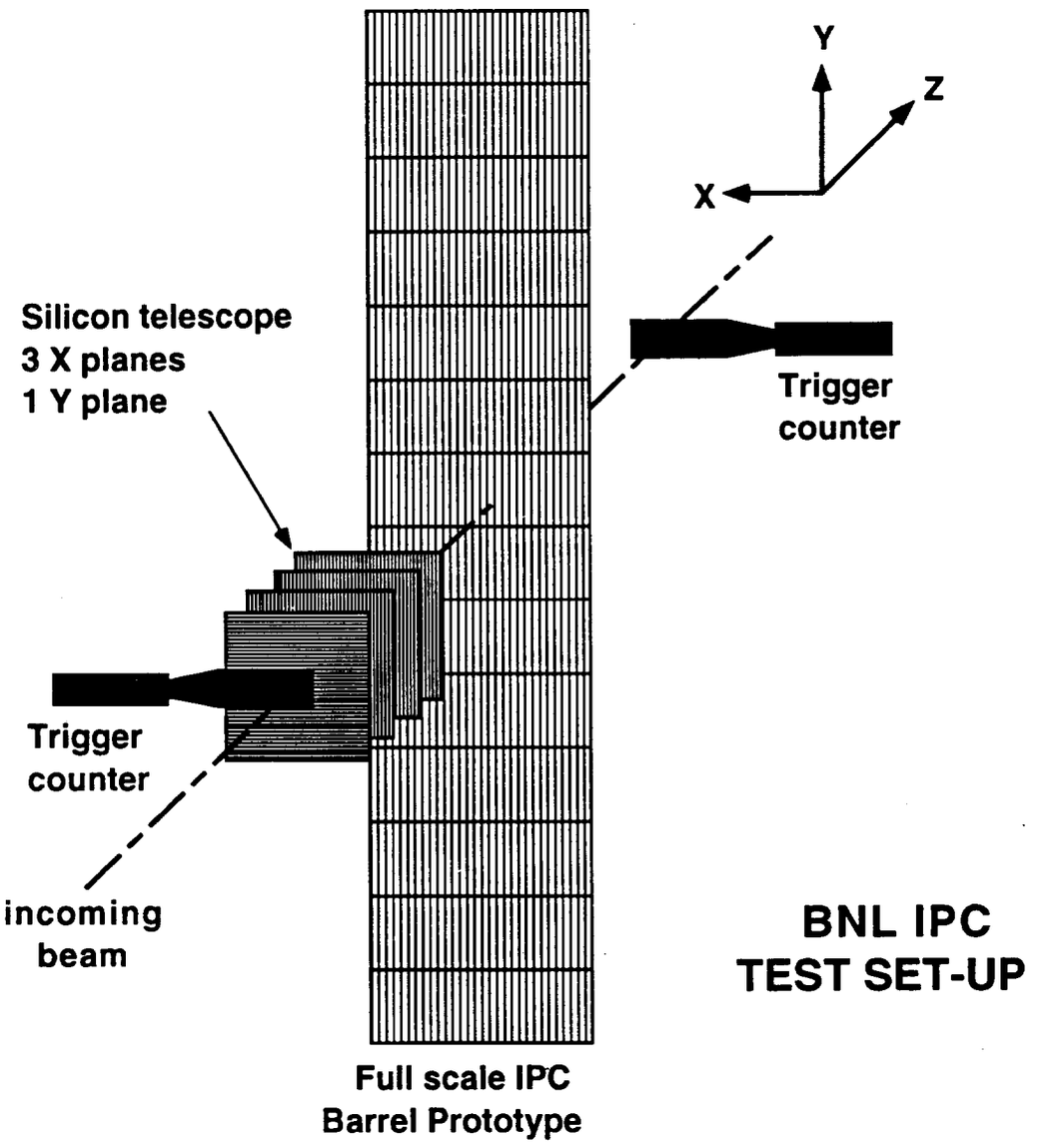

Figure 1: Schematic of the test beam setup.

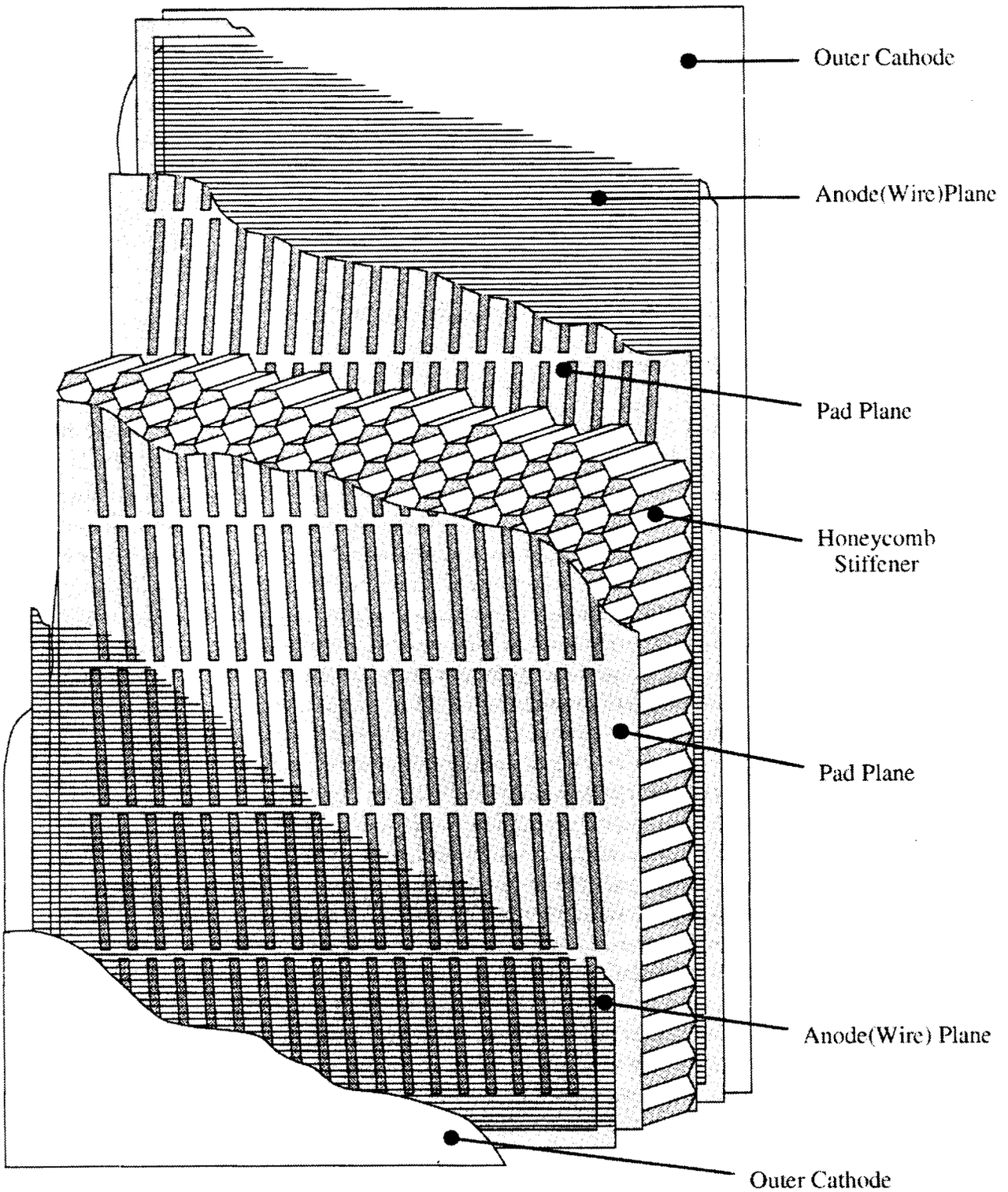

Figure 2: Schematic cutaway view of GEM barrel interpolating pad chamber.

The silicon telescope consisted of three x measuring planes and one y measuring plane as shown in Figure 1. The first silicon plane was the y plane, at z = 0, and the x silicon planes were located at z = 47.6, 111.1, and 150.7 mm. The strips of each silicon wafer were bonded to four SVX chips (128 channels/chip), with gaps in the bonding between the first and second chips and the third and fourth chips. The instrumented length was 1.38 cm in the center of each wafer and 0.69 cm on either side of the center, with approximately 0.2 cm holes in between. The analog levels of all silicon wafer strips were read out by the SVX Readout Sequencer and the SVX Data Acquisition (SRS/SDA) [2] modules for each trigger so that analog interpolation could be used to get the best possible resolution from the silicon planes. The analog levels were read into an 8 bit ADC.

2.2 The Interpolating Pad Chambers

2.2.1 Chamber Description

The structural integrity of the barrel IPC is based on a light NOMEX [3] honeycomb core of 0.635 cm ($\frac{1}{4}''$) thickness, of density 0.029 g/cm^3 with a cell size of 0.3175 cm ($\frac{1}{8}''$) and web size of 38 μm (0.0015″). The honeycomb is sandwiched between two double sided printed circuit boards each of 0.05 cm thickness on which the pads are etched from 1 oz copper on one side and the readout traces on the side nearest the honeycomb. Each etched pad is connected to its readout trace by a plated through hole and the traces extend all the way to the readout connectors at the edge of the board. 1 oz copper was used instead of 0.5 oz because of a technicality related to the plating through of the holes. The total thickness does not exceed 1% of a radiation length. In principle, 0.5 oz copper can be used which would, of course, reduce the radiation thickness of the total chamber. PC boards of 25 cm width and 30 cm length are connected end to end to form a chamber of 2 m length, in order to take advantage of the commercially fabricated PC board size. The layout of the pads and the readout traces are shown in Figures 3 and 4 respectively. The etched pads are 10 cm long, have 2.5 mm pitch and 2.25 mm width and are oriented at a 50 mRad angle to the longitudinal axis of the board in order to achieve, using two pad layers, a two dimensional position measurement. Anode rails made from G10 of 2 mm height (the required anode-cathode spacing) and 2 m length are attached to both PC boards around which the 20 μm gold plated tungsten anode wires are wound in a helical way with 2 mm pitch, thus winding both chambers at the same time with no need for a transfer frame. The anode rails are 2 cm wide, allowing the high voltage and ground distribution circuits to be etched on them. Gas plenums are attached at either end of the chamber to direct the flow of gas, one serving as an inlet and the other as an outlet. These plenums were made from Polyethylene Terephethalate which is a light material with density of 1.0 g/cm^3. In each chamber layer, the gas is directed into the active volume where particle tracks will be read out, and at the same time into the volume outside this which acts as a pressure equalizing volume.

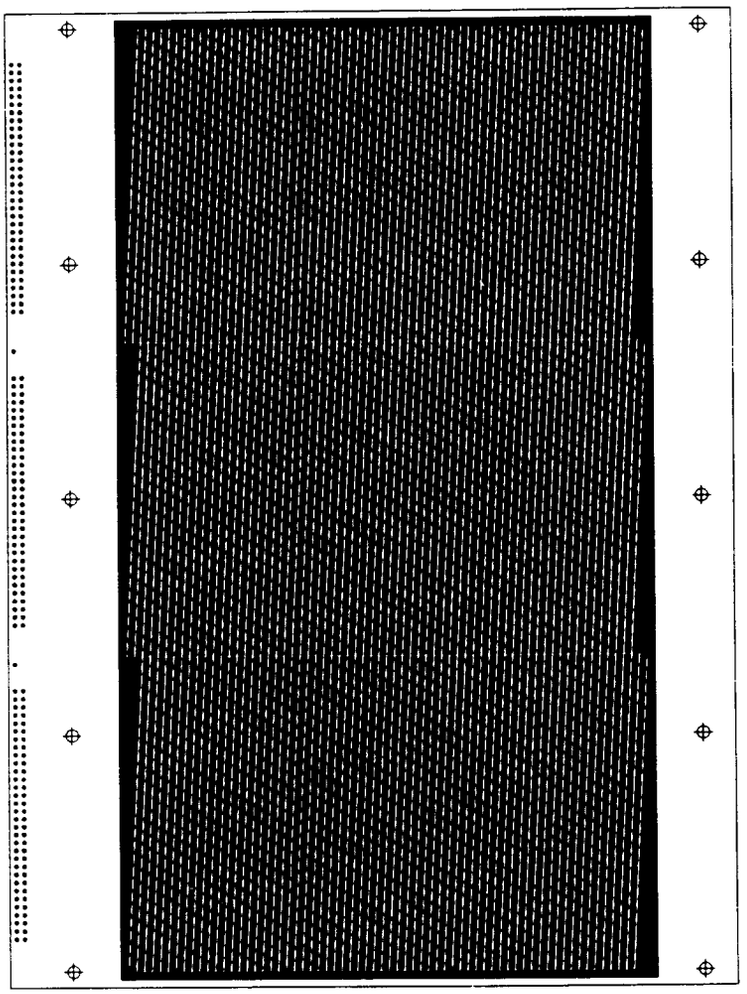

Figure 3: Layout of the etched pads on the PC board. The copper covered an area of 16.8×30.2 cm.

Figure 4: Layout of the readout traces on the PC board. The total area of the PC board was 22.9×30.5 cm.

2.2.2 Chamber Construction

For construction of these chambers, the vacuum bag technique was utilized. A ridged flat surface was made from a 2.3 m long, 0.5 m wide and 2.54 cm thick aluminum plate laid on top of a granite slab of the same area. A straight edged alignment reference bar was placed along the length of the aluminum plate. A steel pin was used to provide the alignment reference along the width of the plate. Two 2 m long PC board "skins" were constructed from several 30 cm long PC boards placed end to end and held together temporarily by tape applied to the pad side. Tape was also used to seal off the plated through holes on the readout side of the PC boards. A mixture of EPON [4] epoxy was applied uniformly to the readout side of the PC board skin which was then laid pad side down on the aluminum plate with the edges placed firmly against the alignment reference bar and the alignment pin. A layer of NOMEX honeycomb was then placed on top of the PC board which extended about 10 cm further than the PC board on the side opposite to the alignment bar in order to avoid damage to the PC board edge by the crushing force of the vacuum bag. A diagram of the construction table is shown in Figure 5. The second PC board skin was then epoxied on the readout side and laid this side down on the honeycomb, again aligning its edges with the alignment bar and the steel pin. This is important in order to ensure that the stereo angle of each layer is properly oriented with respect to the other layer. A second aluminum plate was laid on top of the upper PC board and this was covered with cheese cloth in order to provide a uniform vacuum inside the bag system during the initial moments of evacuation. The whole ensemble was covered by a 0.25 mm thick polyethylene sheet which was sealed to the aluminum plate with a special extra sticky vacuum tape. The vacuum was pumped down to 25 inches of Hg and remained for the duration of the epoxy curing which was about 24 hours. At the end of the curing period, the cathode surface was cleaned and the extending honeycomb was trimmed off.

Printed circuit board techniques were used to etch high voltage and ground distribution circuits on the G10 anode rails. The high voltage distribution circuit consisted of 20 anode wires ganged together to a high voltage bus via a 100 kΩ resistor and a 1000 pF capacitor was placed between the anode wires and ground as shown in Figure 6. Since two rails were used to support the anode wires, one on each side of the chamber, the second rail was used for the ground distribution scheme. A mirror image circuit of the high voltage side was used for the ground side with the resistor replaced with a capacitor and the high voltage bus replaced by a ground bus.

The same vacuum bag procedure was used to attach the anode rails to the PC board skins. OXY-BOND[5] epoxy was evenly coated on one side of the G10 rail and the two anode rails were placed on top of the PC board skin with an alignment plate positioned between them in order to maintain the precise relative position of the rails. They were arranged so that the high voltage rail of one IPC layer was closest to the high voltage rail of the other layer. The aluminum plate was placed over the rails and the vacuum was kept at 25″ Hg for 24 hours by a polyethylene sheet covering the whole chamber.

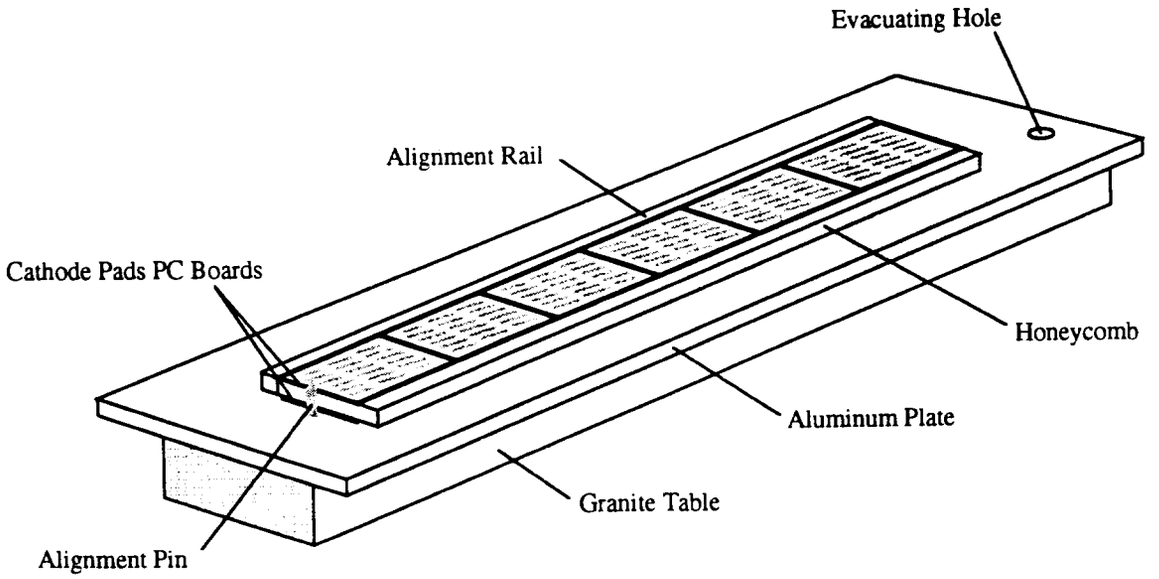

Figure 5: Schematic diagram of the chamber construction table.

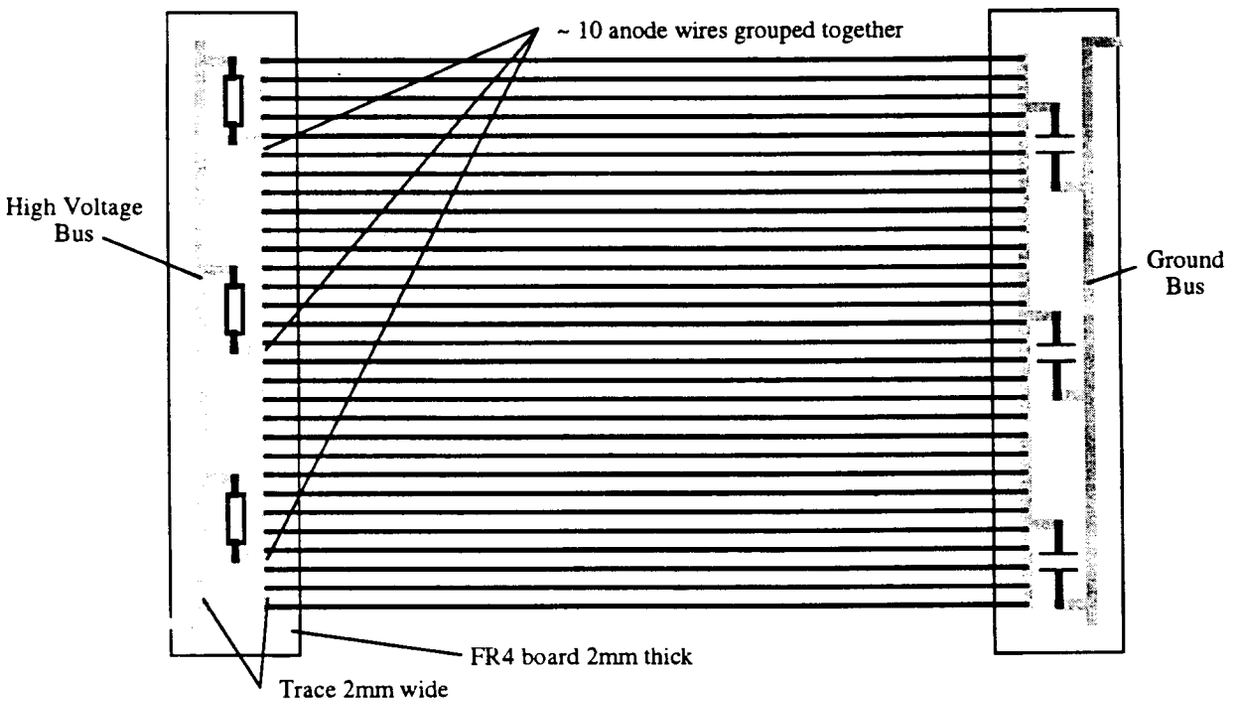

Figure 6: Schematic diagram of the high voltage distribution circuit.

Following this procedure, the gas plenums were epoxied onto the ends of the chamber using OXY-BOND. The gold-plated tungsten anode wires were then wound using a long bed lathe. After the winding, OXY-BOND was applied to the inner edge of the anode rail to hold the wires in place while avoiding the anode wire high voltage pads. 40 μm guard wires were placed at either end of the wire plane. The anode wires were soldered using a low melting point (155°) solder called RHEOMET, consisting of 43% tin, 43% lead and 14% Bismuth. The Cathode rails were then placed on top of the anode rails and epoxied to them using the vacuum bag method. The cathode windows were stretched over and epoxied to the cathode rails. These were made from 2000 Angstrom Aluminum coated on 25 μm thick Mylar. Finally, the gas window rail was epoxied on top of the cathode rail. This rail was made out of a graphite epoxy for additional stiffness which was possible because no high voltage was present in this region. The gas window of single sided aluminized Mylar was stretched over these rails to provide a pressure equalizing region, to avoid distorting or damaging the cathode window with large changes in pressure. A cross sectional view of the constructed chamber is shown in Figure 7.

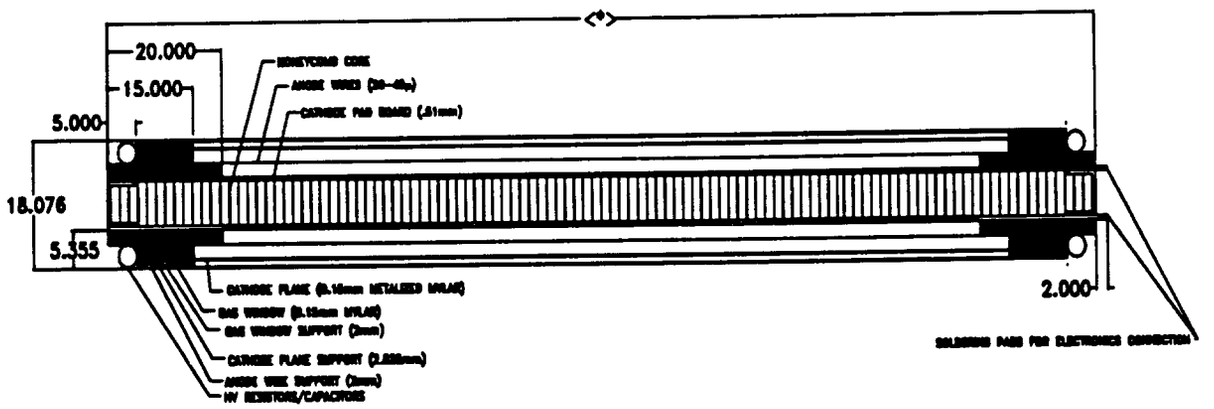

Figure 7: Cross sectional view of the constructed chamber.

2.2.3 Chamber Setup

The pad planes were located at z = 198.3 and 199.0 mm. The particle beam was centered on pads 28–40 near the center of the chamber. The beam profile is shown in Figure 8 as a function of pad number. Gas composed of 50% CO_2 and 50% CF_4 was circulated through the chambers.

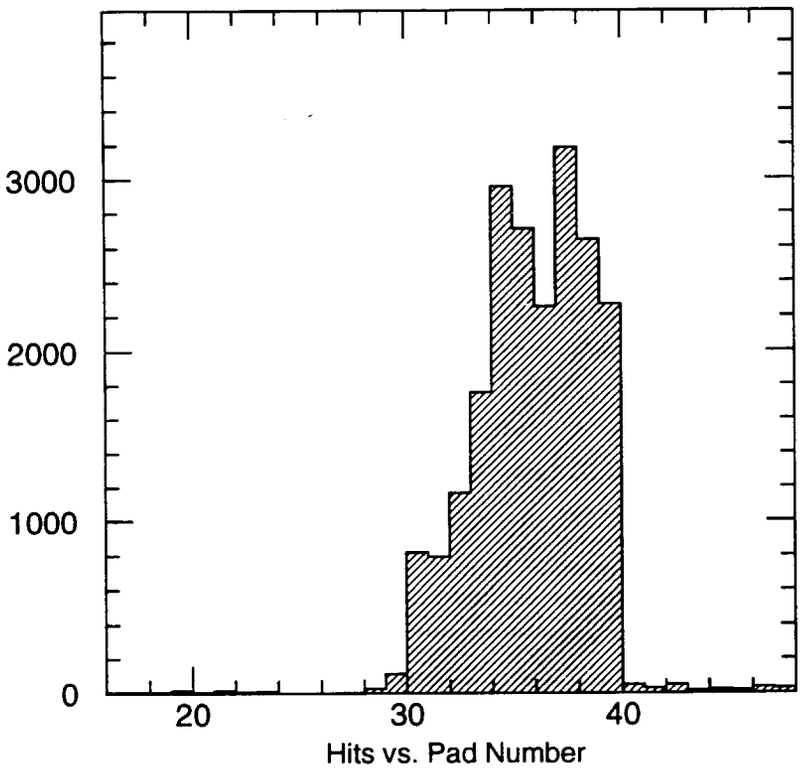

Figure 8: The beam profile as a function of pad number in plane 1.

2.3 IPC Electronics

Each cathode pad signal was input to a GEM prototype preamp-shaping amp pair. These are nominally the same designs as will be used in the full GEM Central Tracker, but with different packaging. The preamp had a BNL model number IO456-4 and the shaping amp was model IO638-01. The preamp inverted the pulse (from positive to negative) and the shaper was non-inverting with unipolar output. The total gain of the preamp-shaper pair was typically 10^5 pC/pC. For a 5 nsec pulser input to the front of the preamp-shaper pair, the output of the preamp and shaping amp had risetimes of 12 nsec and 20 nsec respectively. Both components had falltimes of 20 nsec for this fast pulse input. A 330 pF coupling capacitor between the preamp and shaper controlled the time characteristics of the output pulse for real (i.e. electron avalanche) signals.

The CAMAC data acquisition system was located about 10 meters from the chambers, which necessitated long transmission lines. In addition, the trigger logic delays resulted in additional lines for the amplifier outputs. The total length of twisted pair ribbon cable between the shaping amp and the CAMAC crate was approximately 25 meters. 51 Ω resistors were added in series at the amp end to give the required 100 Ω termination. In addition, 51 Ω resistors were added in parallel at the ADC end in order to halve the pulse size. This attenuation was necessary to keep the pulses on scale in the ADC. Note that the amplifiers have fixed gain, and the chamber voltage, and therefore gain, must be optimized for best position resolution, so changing chamber voltage to reduce signal size is not an option. As a result of attenuation in this cable, the risetimes of the avalanche signals were stretched to 60 nsec. The falltimes of these pulses were about 140 nsec. A reduction in capacitance of the above mentioned coupling capacitor to 100 pF will reduce the falltime considerably, and this change will be implemented for future tests in order to more easily handle high rates.

The amplifier outputs were fed into LeCroy 4300B 11 bit charge integrating ADCs with a nominal full scale charge input of 500 pC. A 300 nsec wide gate was used for the pad signals.

2.4 Trigger

The trigger consisted of two scintillators, one placed in front of the first layer of silicon (upstream) and the other beyond the last IPC layer (downstream). The upstream scintillator was about 2.5 cm square (about the same size as the active portion of the silicon wafers) and the downstream one was 5.0 cm square to take into account possible beam divergence and multiple scattering. The particle flux from the beam was on the order of 10 kHz. The trigger logic is shown in Figure 9.

The sequencer file for the SVX chips was set up so that they would continually cycle through a reset followed by integration of the silicon wafer signal until a coincidence was formed between the integration period of the SVX chips and a trigger formed by the scintillators. If a coincidence was formed, it was assumed that a particle track must have passed through the silicon wafers during the integration period. The SVX chips were then read out, the various ADC gating and readout sequences began to collect the IPC data, and the reset/integration cycle would begin again.

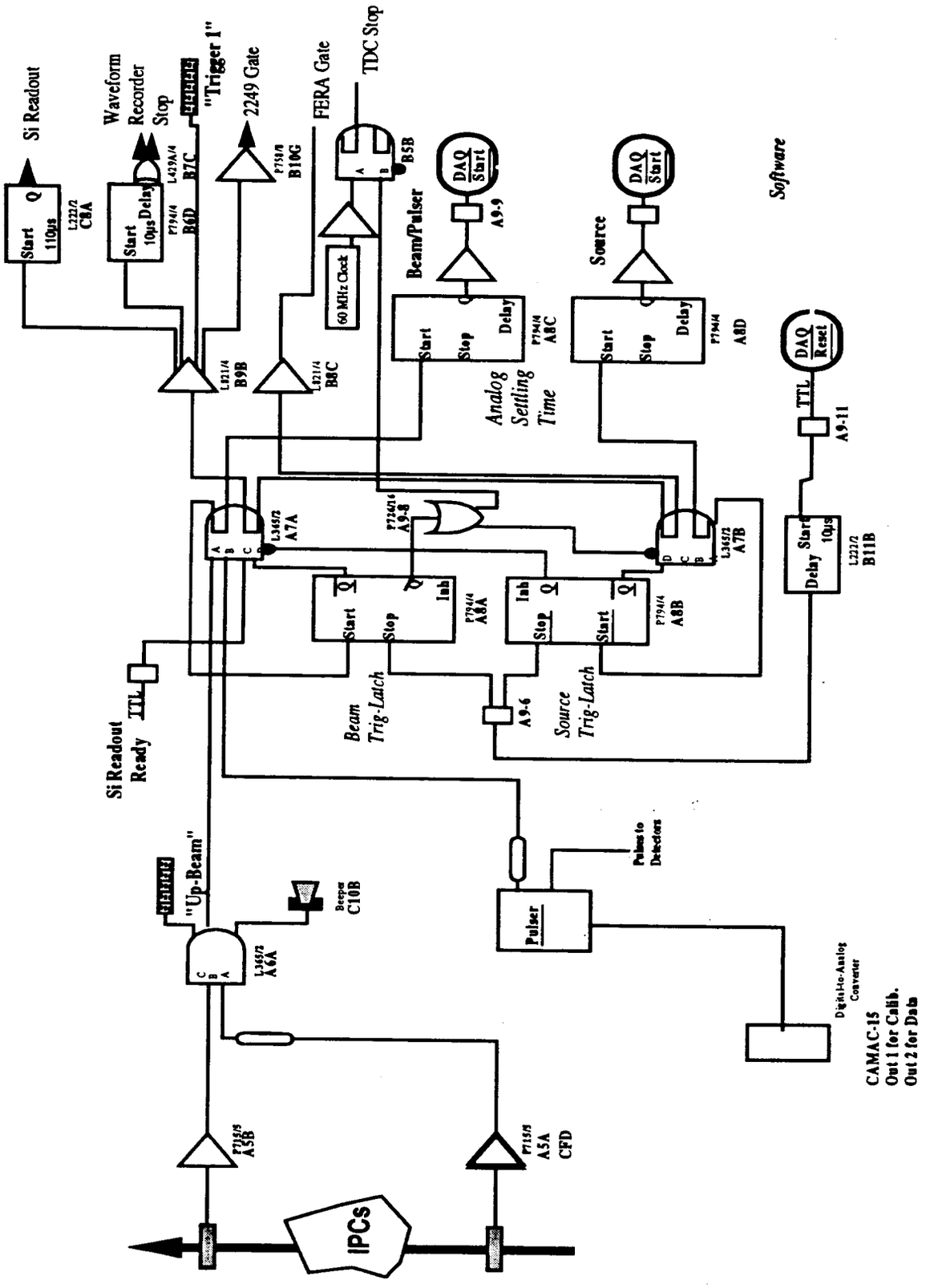

Figure 9: Trigger logic.

2.5 Data Acquisition

The SSCL DAQ system developed for the Texas Test Rig [6] was implemented in the BNL beam test. The hardware configuration consisted of 2 VME processors, a digital I/O card in VME, and a Jorway model 73A CAMAC-SCSI crate controller. One VME card, an MVME-162 with an embedded Motorola 68040 processor, performed frontend readout and event building. CAMAC was directly accessible to the 68040 at its SCSI port via the SCSI bus interface provided by the Jorway controller. Events were buffered in 68040 memory and subsequently transferred over the VME backplane to a FORCE computers SPARC CPU-2CE for monitoring and display, then recorded to an attached EXABYTE model 8500. The VxWorks realtime kernel in the 68040 provided high readout rate capability while the combination of the SPARC CPU, SUN OS 4.1.2 and a 2 Gbyte SCSI disk provided the full functionality of a UNIX workstation with a software environment similar to the Physics Detector Simulation Facility (PDSF) at SSCL.

The event recording rate for the full setup was 8 Hz with an event readout time of 26 msec. Calibration runs and other specialized data runs not requiring silicon information were read out at rates of 400 Hz and benefited from the real time performance of the 68040 processor. For full readout the silicon detector dominated the readout time but, overall, readout time was not the limiting factor. Rather, deadtime in the trigger limited the recording rate. The trigger deadtime was again dominated by the silicon detector, which was operated with a live integration interval of 6.2 μsec, chosen to suppress the incidence of two beam particles in the same event In the absence of a triggered event, each 6 μsec integration interval was followed by a reset and precharge interval during which triggers were disabled. The event size was 8.4 Kbyte consisting mainly of the 2048 channels of silicon data. Both analog and digital data, in the form of a chip ID and channel address, were recorded. Seventy-two channels of analog data from the IPC's were digitized in 11-bit LeCroy model 4300B FERA ADC's. A total of 295 K events with silicon and IPC information were recorded for resolution studies.

A number of calibration runs were recorded with the IPC frontend electronics pulsed by a DAC-controlled pulser. Seventy thousand events of IPC data were recorded in a high-voltage scan at 7 points between 2625 V and 2775 V.

A second VME sparc card (2LC from Themis computers) with an independent 2 Gbyte SCSI disk was configured as a backup to the DAQ SPARC. It was used for offline analysis and hosted an Apple laserwriter printer.

2.6 IPC Gas System

Because of the high cost of CF_4, a recirculating gas system was chosen to supply an equimolar mixture of CO_2CF_4 to the IPCs. The flow was contained inside the IPCs

by 25 μm thick Mylar films which make up the gas windows which can withstand up to 5 Torr pressure differences. The gas composition was monitored for trace contaminants to 1% accuracy at several ppm. A gas scrubbing subsystem filtered out water vapor, O_2 and total hydrocarbons to low ppm levels. Pressures at five locations and temperatures at four were continuously monitored. Concentrations of oxygen and moisture were maintained under 10 ppm and 1 ppm respectively during continuous operations over a period of 100 hours.

3 Data Analysis

3.1 Silicon Analysis

3.1.1 Baseline and Pedestal Noise Subtraction

In order to find hits in the silicon detectors, it was necessary to search for one or more adjacent strips which were above some threshold. Actually, the signals from the silicon are negative but in the following discussion they will be treated as absolute values. This threshold was calculated for each channel after the data had undergone baseline noise subtraction. Baseline noise refers to event by event fluctuations in which all of the strips changed pulse height by approximately the same number of ADC counts which had a value of about 140 ADC counts as shown in Figure 10. Such fluctuations were measured by calculating the average strip pulse height for all strips on each SVX chip. This baseline was then subtracted from the raw data on an event-by-event basis. The pedestals for each SVX channel were calculated with baseline subtracted data by calculating the average pulse height of each strip over 50 events. Figure 11 shows the pedestal for each silicon plane. The pedestals can be seen to change sharply in magnitude from one 128 channel SVX chip to the next. The baseline and pedestal subtracted pulse heights were used in the cluster search. Figure 12 is a profile plot of the pedestal and baseline subtracted data versus strip number.

3.1.2 Cluster Finding Algorithm

A cluster was defined as one or more adjacent strips above the appropriate threshold. Clusters were searched for in the silicon using the pedestal and baseline subtracted data. Dead strips and strips that were above the threshold cut more than 5% of the time were removed. To find a cluster, a "seed" strip was required with an ADC value greater than N times the rms ADC value of the strip, where N was defined separately for each SVX chip. Because the last plane was noisier, as can be seen in Figure 12, a looser cut was imposed on it to obtain better efficiency. For the seed strip the cuts

chosen were 3.5, 3.5, 3.5 and 2.5 sigma above noise for the 1st, 2nd, 3rd and 4th planes of silicon respectively. If a seed strip was found the neighboring strip was required to pass a cut at 3.0, 2.5, 2.5 and 2.0 sigma above noise for each of the planes respectively, if it was to be included in the cluster. When a neighbor strip failed the cut no more strips were included in the cluster on that side of the seed strip. The center of gravity of the cluster was then calculated. Figure 13 shows the pulse height distribution for strips that were used in clusters showing the characteristic Landau distribution, with a small noise peak around zero. Figure 14 shows the center of gravity of the cluster position. A lower number of clusters was found in the fourth plane as expected from the higher noise in this plane. The apparent holes in the distribution correspond to strips which were not instrumented.

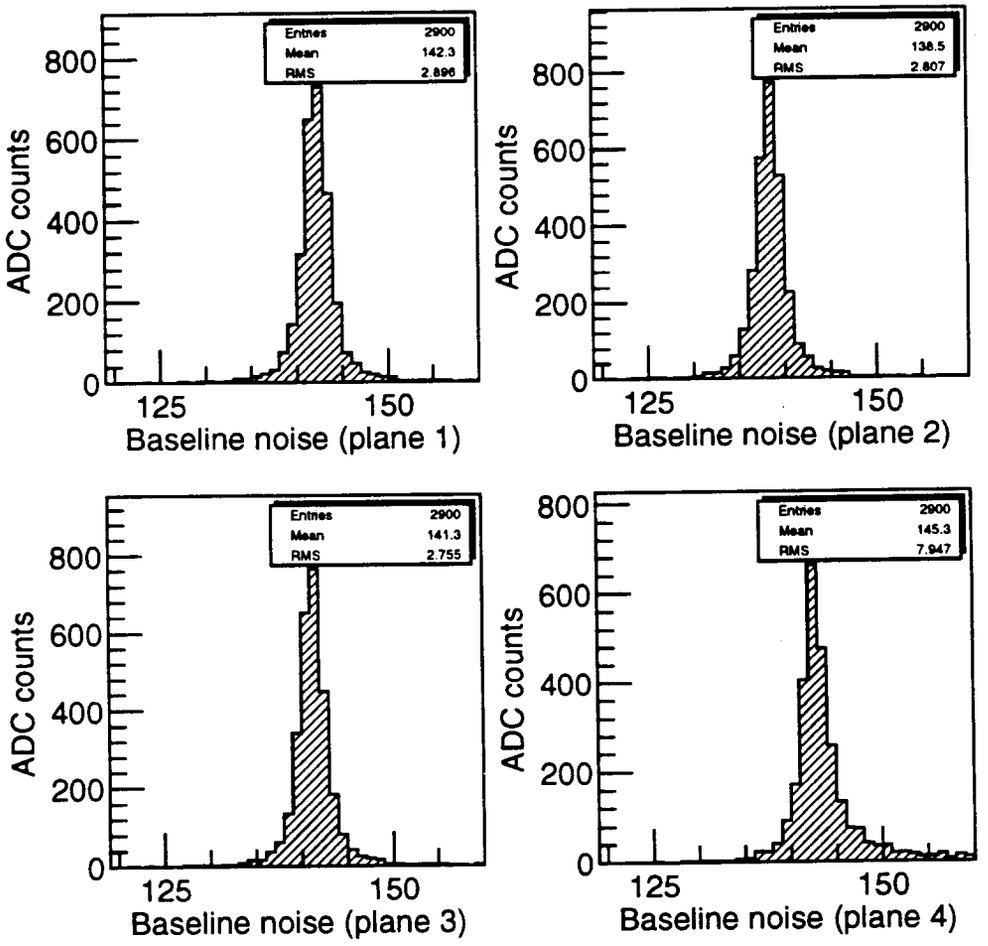

Figure 10: Measured baseline noise for one run for each of the four silicon planes. To convert the rms value into equivalent electron charge, the factor is 480 electrons/ADC channel. This does not take into account any offset in the ADC, and so should only be applied to the rms width.

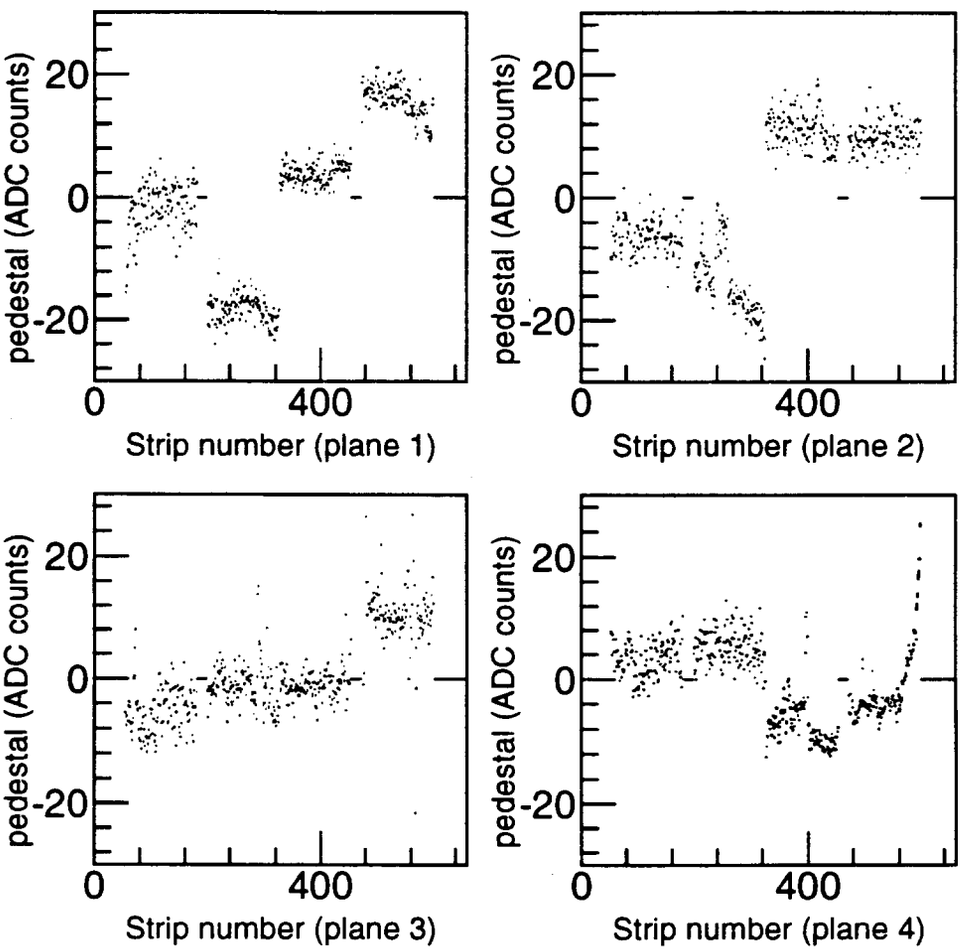

Figure 11: Average pedestal after baseline subtraction as a function of strip number for the four silicon planes. The boundary between each 128 channel SVX chip is clearly visible.

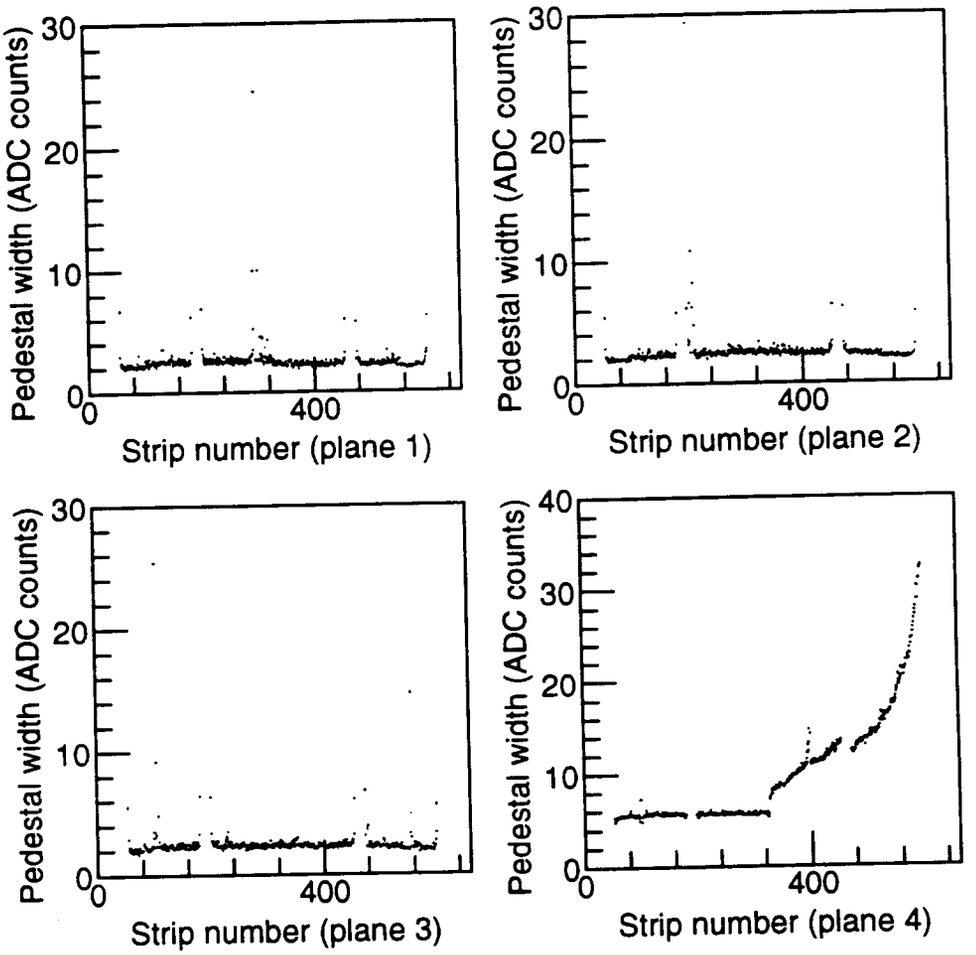

Figure 12: Baseline and pedestal subtracted rms ADC pulse heights versus strip number in the four silicon planes. Use the factor 480 electrons/ADC count to convert ADC counts to equivalent electron charge. The fourth plane can be seen to have rather more noise in the second two SVX chips.

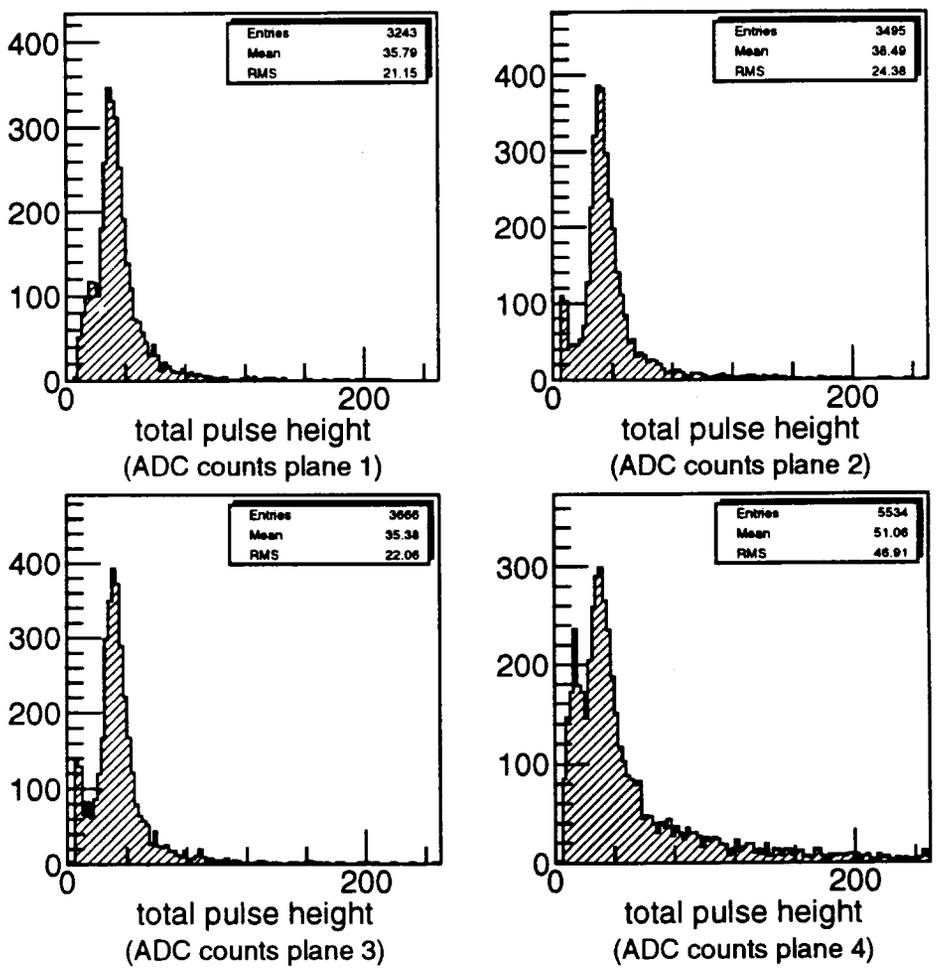

Figure 13: Total pulse height in a cluster in the four silicon planes.

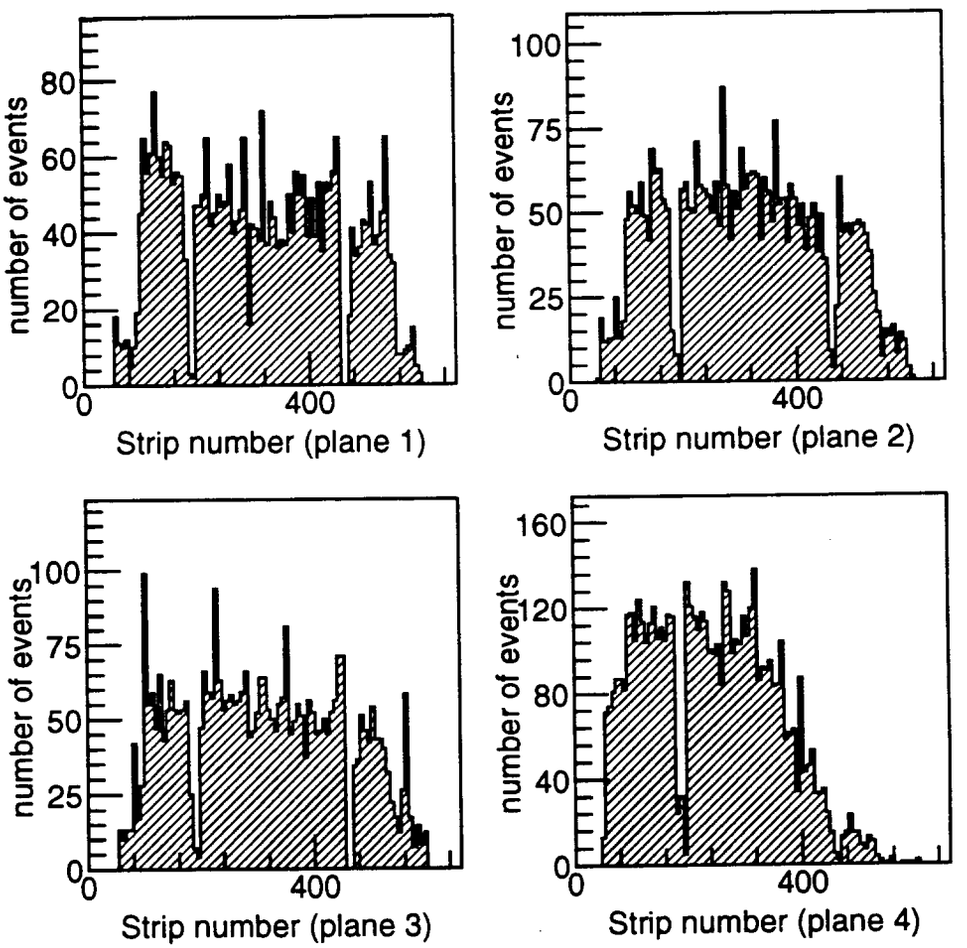

Figure 14: Found cluster center of gravity in the four silicon planes. The regular gaps in the distributions correspond to strips which were not instrumented.

3.1.3 Alignment of Silicon

After the clusters in each silicon plane had been converted into local coordinates, they were first used to reconstruct tracks to be used for alignment of the silicon telescope planes. A set of coordinates was selected as a candidate track if there was a coordinate formed in all three of the silicon x planes, and if the difference in measured x values between the three planes was less than 500 μm. The coordinates were then used in a linear least-squares fit where the slope and offset of the track as well as the chi-square value for the fit were determined. Using the data consisting of tracks traversing all four planes of silicon, it was possible to align the silicon wafers to about 1 μm in x, about 5 mRad in θ_{xy} and about 10 mRad in θ_{xz}. These accuracies were ascertained using a simulation of the setup. Figure 15 shows the mean of the residual as a function of y before and after the alignment correction for all three silicon x planes. A straight line fit to these distributions yields the angle in xy as the slope and the offset in x as the constant. See Table 1 for the values of these constants. Shifts in coordinates of second order importance (z, θ_{yz} and θ_{xz}) were measured using a more general minimization technique where the coordinate axes are defined by the x position of the first and third layers and θ_{xy} and θ_{xz} are defined by the first layer also.

3.1.4 Silicon Resolution

In order to understand the effects of multiple scattering in the beam test which are important due to the relatively low beam energy of 8 GeV, a Monte Carlo program was developed. The position error due to multiple scattering was found to be 5 μm and 8 μm in the 2nd and 3rd silicon x planes respectively. The effects of multiple scattering in the first silicon plane, which only measures the y position, does not enter the fit. The projection error of the silicon track due to the combined effects of multiple scattering and silicon resolution was calculated in the 1st and 2nd IPC planes to be equal to 12.0 μm and 12.5 μm respectively.

Figure 16 shows the residuals for each silicon plane for a weighted line fit to the found clusters. The criteria imposed on these clusters was that they be within 500 μm of each other in the x direction for all three planes and that the χ^2 of the fit be less than 2. The residuals are smaller than the intrinsic resolution of the detectors in planes 1 and 3 because the fit constrains the outer layers more strongly.

To estimate the efficiency, exactly one cluster was required in each of three silicon planes and the fourth plane was examined for a cluster. Figure 17 shows the normalized number of hits found in each plane. The efficiency is the percentage of times that one or more hits was found in that strip. The four silicon planes had hit efficiencies of 87, 96, 98 and 68%. Included in the efficiency determination was the silicon efficiency and the cluster finding algorithm efficiency which was determined by the signal to noise ratio in each plane.

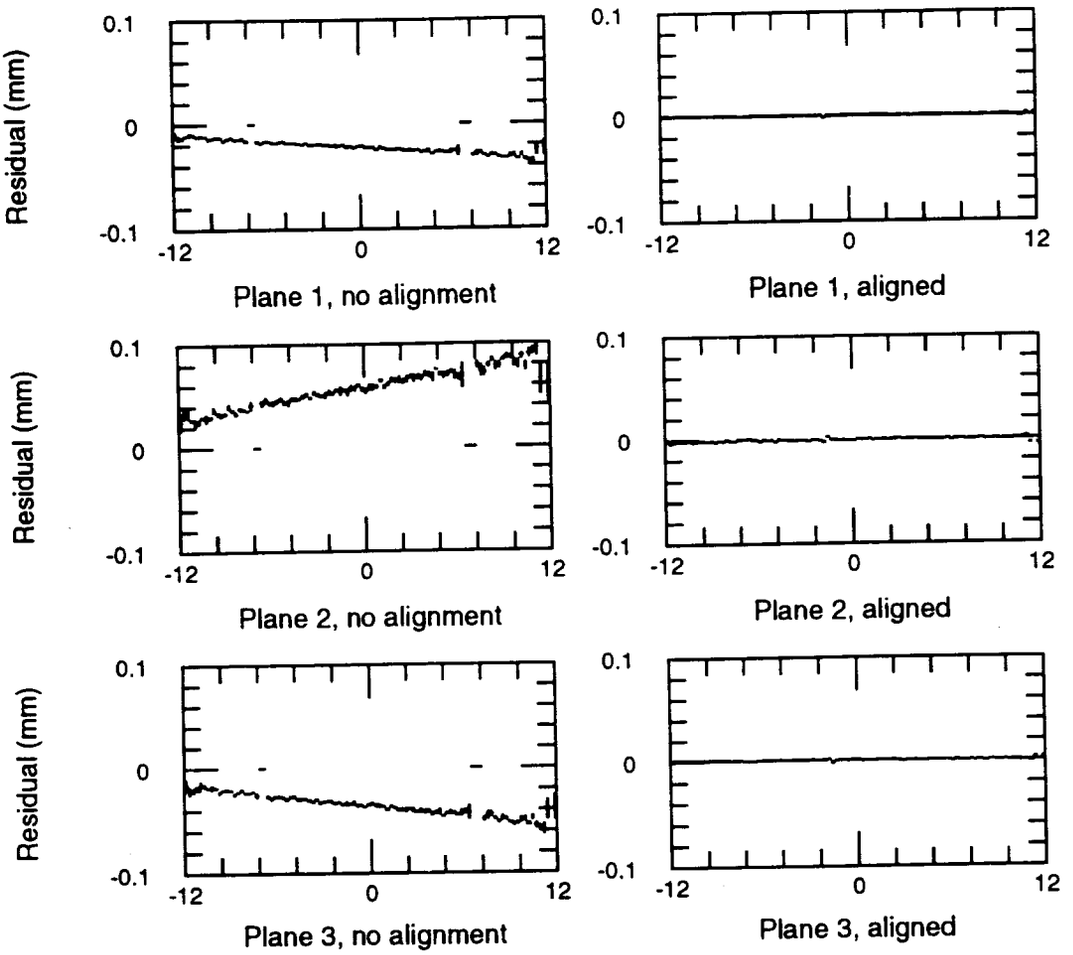

Figure 15: The residuals for the three silicon x layers as a function of measured y position before calibration of the alignment and after alignment. Straight line fits to the data before and after alignment yield the slopes and offsets shown in Table 1.

	no alignment		aligned	
Plane	offset	slope	offset	slope
1	−.2258E−1	−.1045E−2	.3066E−3	−.2832E−4
2	.5872E−1	.2718E−2	−.7909E−3	.7367E−4
3	−.3613E−3	−.1673E−2	.4886E−3	−.4533E−4

Table 1: The results of the straight line fits to the Silicon residuals as a function of y.

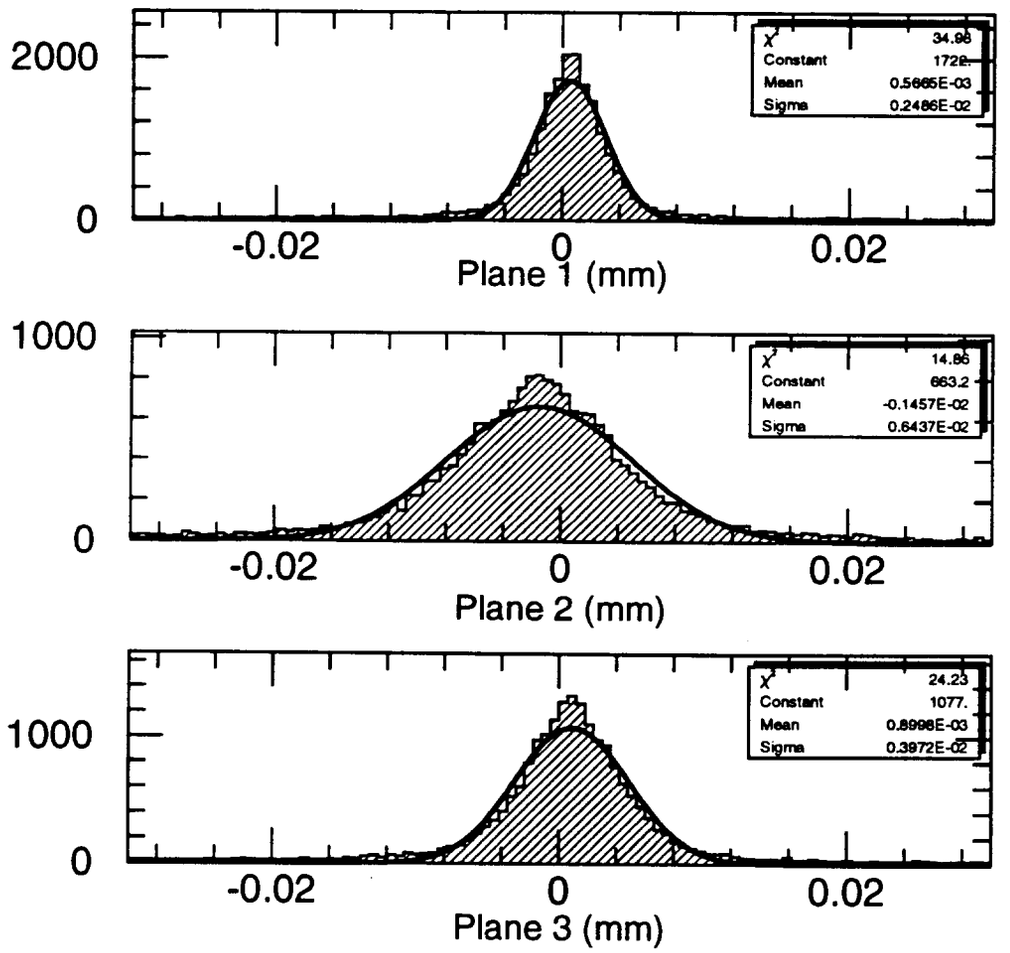

Figure 16: The residuals for the three silicon x layers with Gaussian fits to the distributions. The residuals are calculated relative to a straight line fit to hits in all three planes.

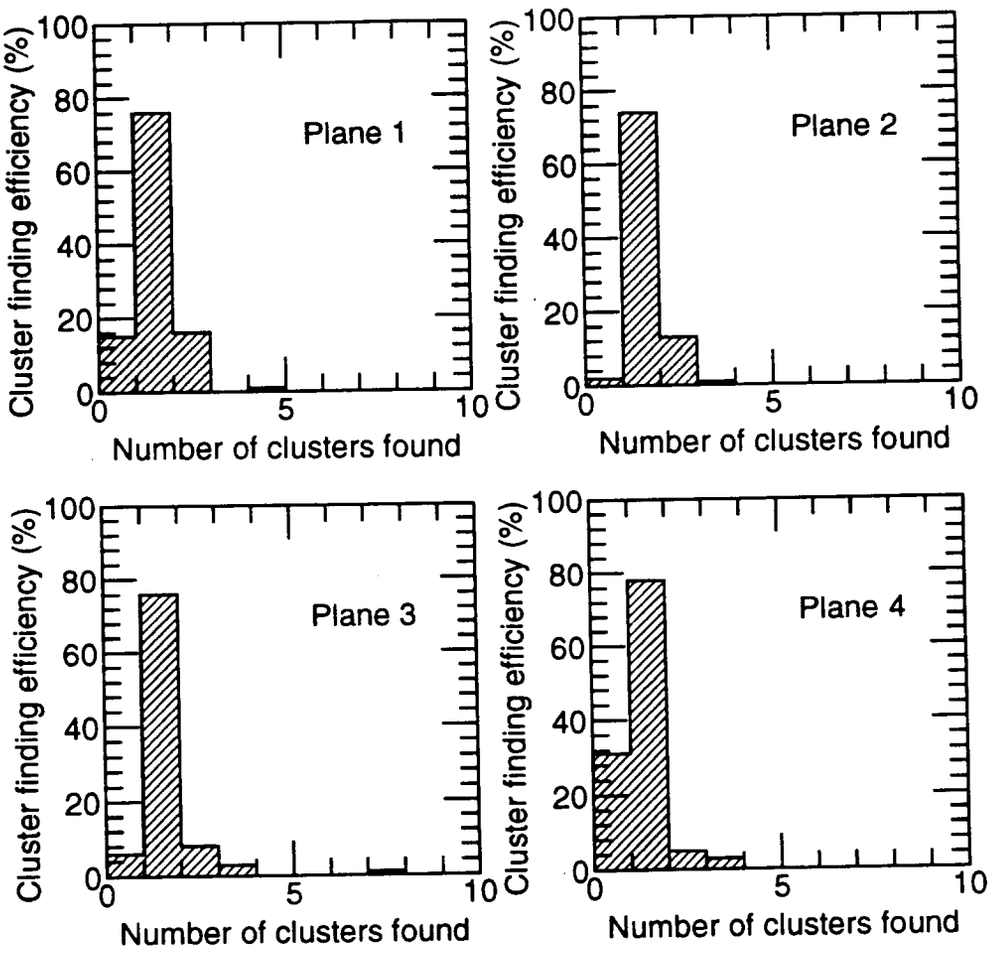

Figure 17: The cluster finding efficiency for each of the four Silicon planes.

3.2 Interpolating Pad Chamber Analysis

3.2.1 IPC Coordinate Measurement

The calibrated pad signals were first scanned to find three contiguous pads with a signal higher than 3σ above zero, where σ is the measured width of the pedestal for that channel. A best estimate of the true track position was then determined by solving the function due to Mathieson [7] to the three pulse heights. This function parametrizes the electrostatics of the chamber geometry for a point charge at the wire. The charge density, $\rho(\lambda)$, on the cathode at a distance $\lambda = (x - x_0)/h$ measured parallel to the anode wire is:

$$\frac{\rho(\lambda)}{q_a} = K_1 \frac{1 - \tanh^2(K_2\lambda)}{1 + K_3 \tanh^2(K_2\lambda)} \tag{1}$$

where

$$K_1 = \frac{K_2\sqrt{K_3}}{4\tan^{-1}\sqrt{K_3}} \tag{2}$$

and

$$K_2 = \frac{\pi}{2}\left(1 - \frac{\sqrt{K_3}}{2}\right). \tag{3}$$

where q_a is the net anode charge and h is the anode-cathode separation. Data analysis of real events resulted in a best fit value of 1.06 for K_2. Inserting this empirical value for K_2 into equation 3 results in a value of 0.43 for K_3. The hit position as determined by this fitting procedure can be compared with the track projected from the silicon in order to probe the resolution of the IPC.

3.2.2 IPC Gain Versus Voltage

The pulse height distributions for both IPC planes at a voltage of 2625 V are shown in Figure 18. Both distributions show the expected Landau shape. The logarithm of the mean of the pulse height distributions versus detector voltage for the two IPC planes is shown in Figure 19 and can be seen to increase approximately linearly with detector voltage as expected in this voltage region.

3.2.3 IPC Alignment

The alignment constants of the IPCs were determined using the data tracks in much the same way that those for the silicon detectors were found. Tracks were reconstructed in the silicon detectors and projected into the IPCs. A minimization of the difference between the found and the projected position was carried out allowing the degrees of freedom involving the x dimension (x, θ_{xy} and θ_{xz}) and also the z position of the chambers to vary. The accuracy of this method is found from simulation to be 5 μm in x and 10 mRad in θ_{xy}. Due to the relatively small beam size, the accuracy of θ_{xz} from this method was less than from the physical placement accuracy which was estimated to be less than 10 mRad.

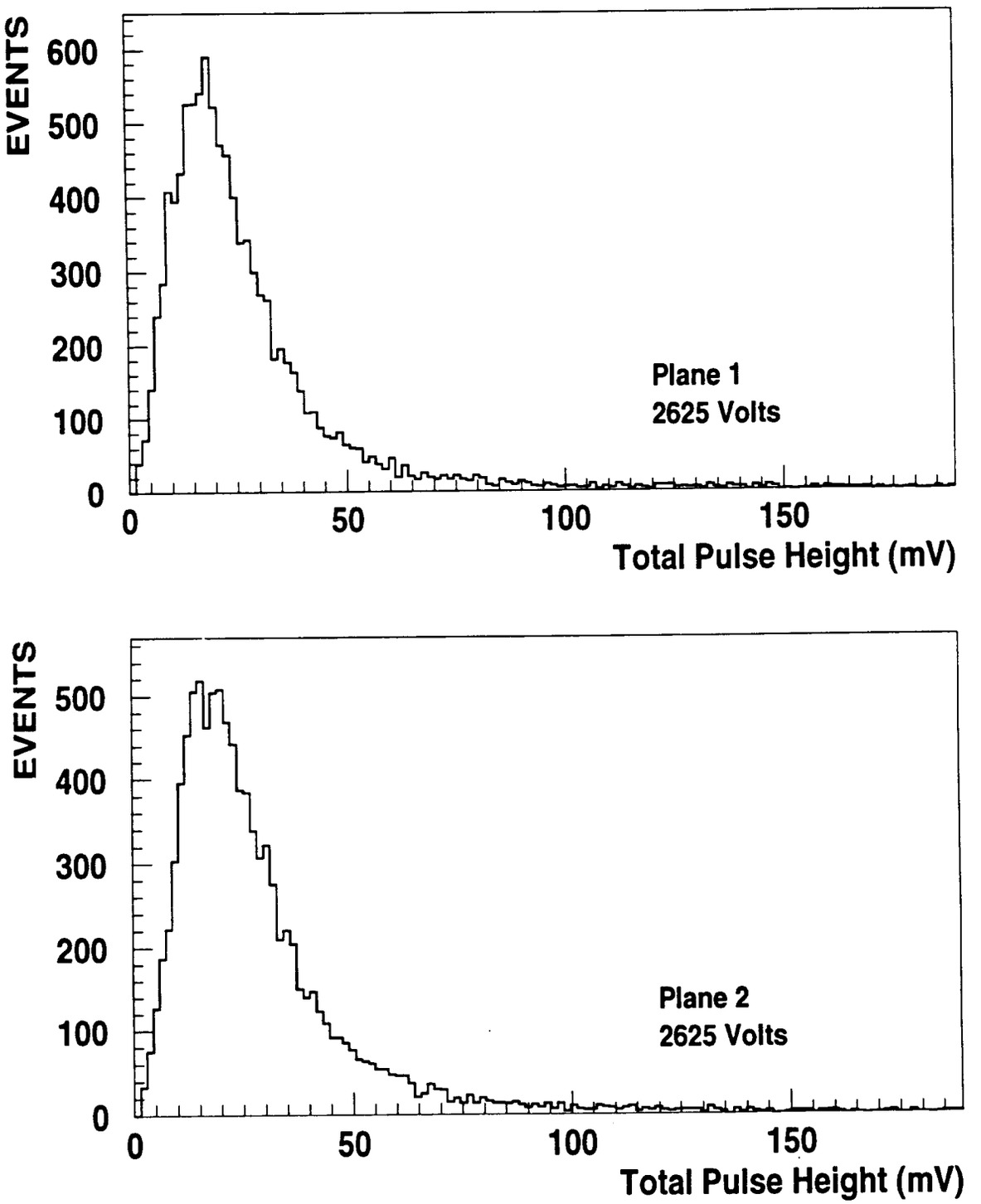

Figure 18: The pulse height distributions for planes one and two, for detector voltages of 2625 V.

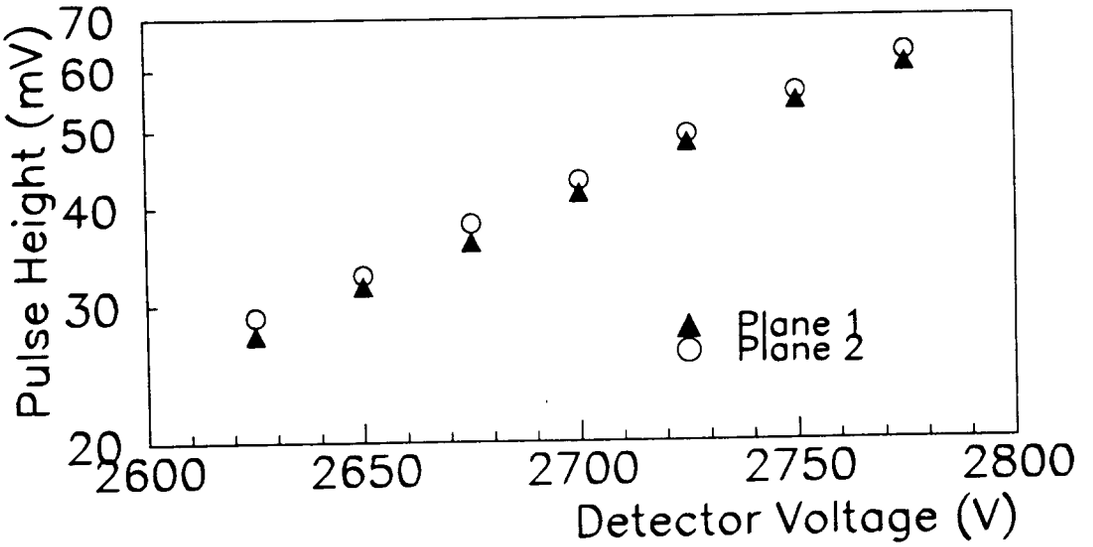

Figure 19: The mean pulse height versus detector voltage for the two planes of the full size barrel Yale prototype.

3.2.4 IPC Calibration

The calibration procedure was composed of two steps. The first step was performed in hardware. A capacitively coupled strip located under the signal lines to the pads was pulsed at 21 different pulse heights and the resulting signals were read out through the electronics chain. One hundred events at each pulse height were recorded. Calibration relations, consisting of a slope and an intercept, were determined for each channel. These relate ADC counts to the corresponding pulser output voltage. This gave a measure of the electronics channel to channel variations. The absolute calibration of the pads is not necessary: only the ratios of adjacent channels are important in the coordinate finding procedure. The signals referred to in the subsequent text have been translated into equivalent mV signals from the calibration pulser.

The variation about the mean for each point gives a measure of the noise. The intercepts did not correspond to the pedestal because the ADCs were non-linear very close to zero and so pedestals were measured with a dedicated pedestal run with no beam present and an auto-trigger. The average pedestal for each pad is shown in Figure 20. The sigma of the pedestal is represented by the size of the error bar. Each channel underwent a pedestal subtraction and a conversion into mV for use in the track analysis.

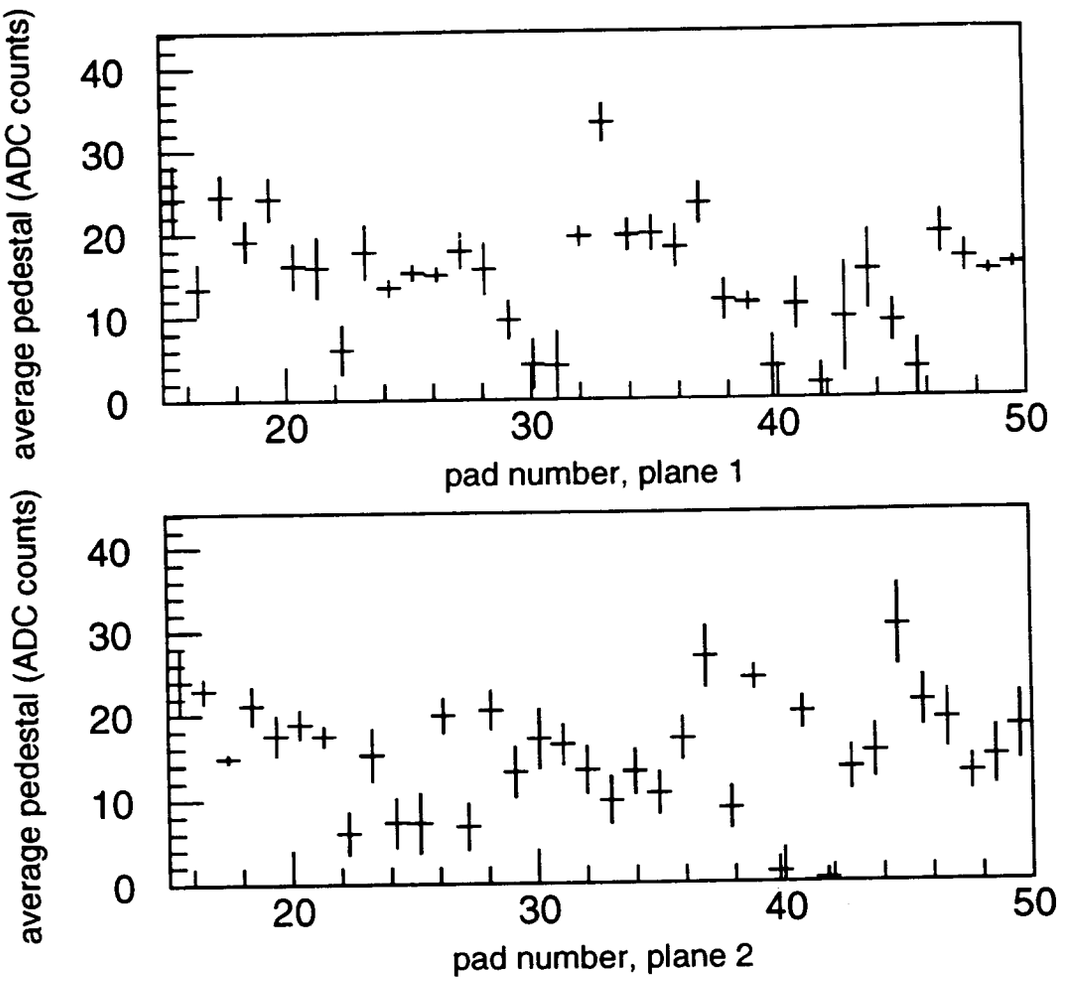

Figure 20: The IPC pedestals. The sigma of each pedestal is represented by its error bar.

After this procedure, upon examination of the residuals for each pad, offsets as large as 140 μm from zero were apparent as can be seen in Figure 21. This indicated that the presence of systematic effects which were not accounted for by the calibration procedure. The sources of these shifts could have been the irregularities in the pad etching procedure, pad to pad variations in capacitance or non uniformity in the distance between the pulsing conductor and the signal lines. Simulations showed that any one of these potential sources could lead to the observed effect. Other effects such as cross talk have not been separately estimated. The resolution is clearly a product of the residual width and its offset from zero. Ideally, the offset should be zero but changes of 2–3% in the gain or active size of a pad can lead to offsets in the residuals of a few tens of microns.

It was found that a further calibration which used track data could improve the system performance. Information from the silicon about the position of the incident track on the pad was used to predict the ratio of the pulses expected on the pads on either side of the central (hit) pad. The absolute size of the signals on the side pads was estimated by normalizing them to the center pad using the Mathieson function. A slope and intercept for each channel was measured relative to its neighbor on the left and separately to its neighbor on the right. Figure 22 shows the predicted versus measured pulse height for pad number 31 as predicted by pad 30 and by pad 32. The relationship is clearly linear with a small but non zero offset.

These relationships were measured for each pad, and so there was associated with pad N, two slopes and two offsets which will be referred to here as m_L, m_R, c_L and c_R, where L and R refer to the pad on the left or the right of center respectively. y refers to the predicted pulse height and x refers to the measured pulse height.

$$\frac{y_L^N}{y_C^{N+1}} = \frac{m_L^N x_L + c_L^N}{m_C^{N+1} x_C + c_C^{N+1}} \tag{4}$$

and

$$\frac{y_R^N}{y_C^{N-1}} = \frac{m_R^N x_R + c_R^N}{m_C^{N-1} x_C + c_C^{N-1}} \tag{5}$$

The subset C refers to the center pad. $m_C = 1$ can be defined but c_C is as yet unknown. It can be estimated:

$$y_R^N = (y_C^{N-1})\mathcal{M}_d = (x_C + c_C^{N-1})\mathcal{M}_d = m_R^N x_R + c_R^N \tag{6}$$

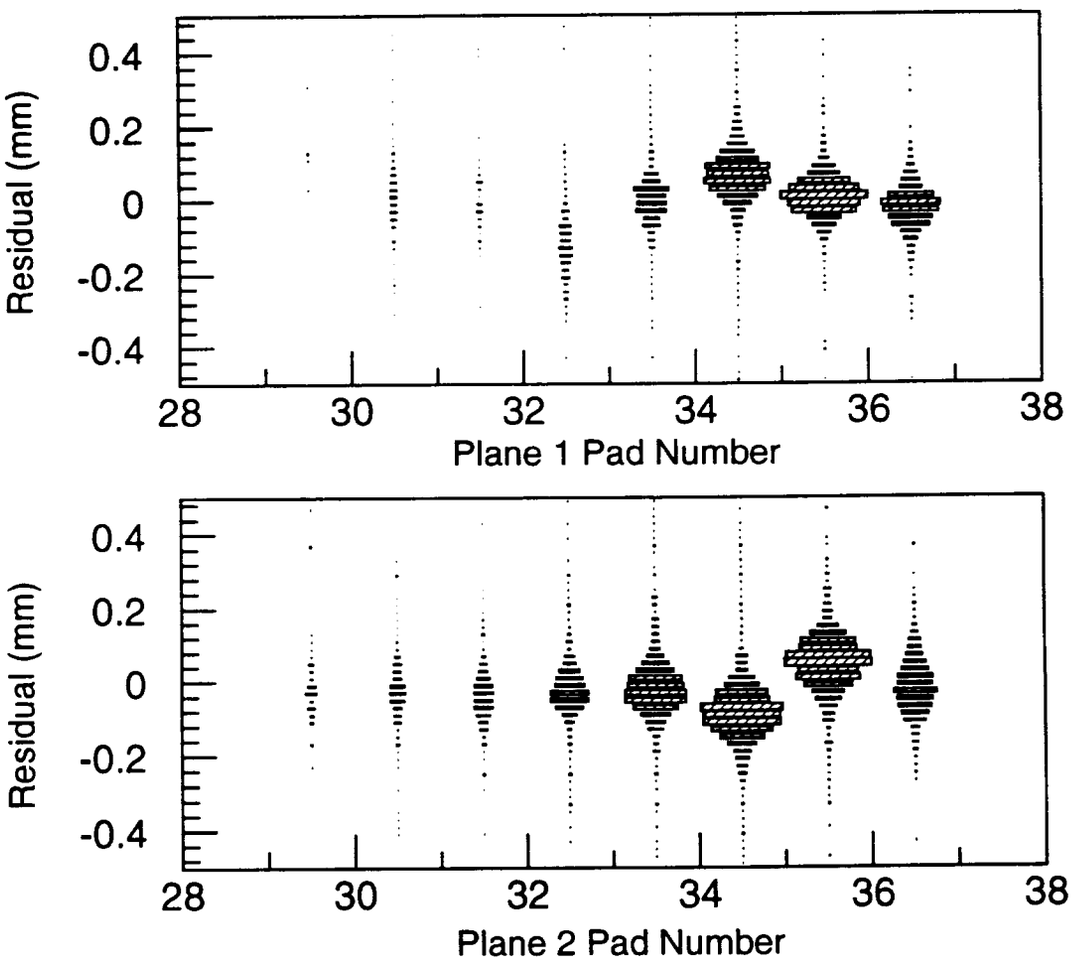

Figure 21: The resolution of IPC plane 1 and plane 2 versus pad number before the software calibration procedure.

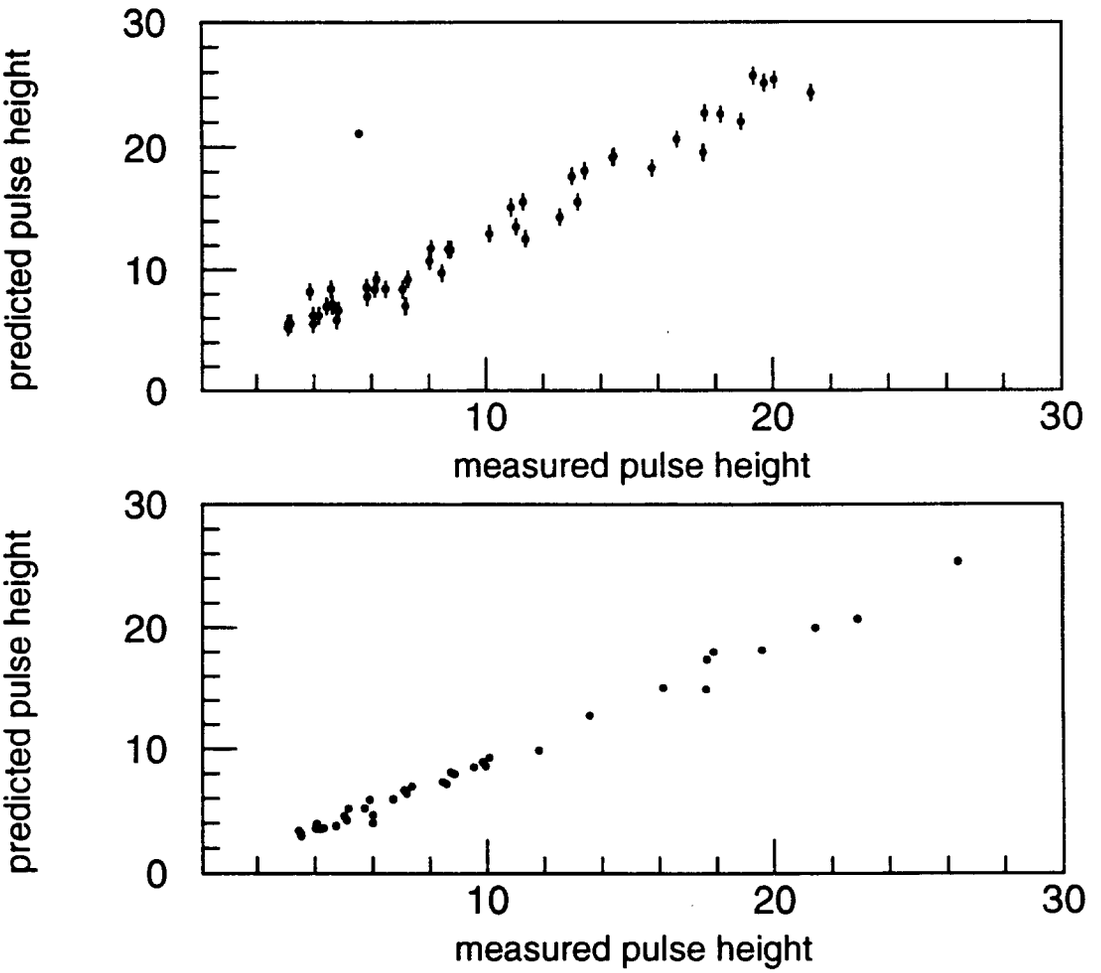

Figure 22: The predicted versus measured pulse height values for pad number 31. The top figure is when pad 31 is on the left of the center pad, and the bottom figure is when pad 31 is on the right of the center pad.

where $\mathcal{M}_d$ refers to the Mathieson function prediction of the pad charge ratio at a distance d from the center of the pad, our best estimate of the electrostatics of the situation. Figure 23 shows the value $\mathcal{M}_d$ as a function of the position across the center pad. Selecting data with $\mathcal{M}_d$ smaller than 0.3 retains more than half the data (for a uniformly populated pad) as shown in Figure 23, but keeps the average value of $\mathcal{M}_d$ to about 20%. Therefore, c_R^N is affected by the uncertainty in c_C^{N-1} by only 20% of the value of c_C^{N-1}.(This cut was used only for the calibration procedure to measure the slopes and offsets for each pad.) It is then possible to use either c_L^N or c_R^N as an estimate of c_C^N good to 20%, for any pad N.

One iteration to improve the estimate of c_C^N proved sufficient. In the simulation, c_L^N and c_R^N were always the same, but in the data, it was necessary to take the average of these two constants to provide the best estimate of c_C^N.

After the calibration was complete the offsets of the residual distributions for all pads were close to zero as can be seen from Figure 24. It is estimated that our calibration of pad to pad differences is about 3% by comparison with simulation although this figure was very difficult to estimate due to the very small number of pads and the fact that more than one set of starting conditions can give rise to the same behavior in the residuals.

4 Results

4.1 Data Cuts

Several cuts were applied to the data that were accepted by the trigger before analysis was performed.

All data in which at least one of the IPC pads involved in the cluster was saturated were cut so that the resolution would not be degraded because of an improperly measured charge distribution. All events which were missing a hit in any of the four silicon planes or either of the pad planes were discarded. The fraction that failed this cut varied in the silicon from 20% of the events on the first three planes to 36% for the last plane. Also discarded were events which had more than one hit in the silicon y plane (since it provided the sole y measurement) or greater than one hit in either of the IPC planes. Once a track was found from the silicon clusters the event was thrown away if the track fit had a χ^2 greater than 2. Finally, the IPC data were checked to make sure that the pulse heights in the center five pads had the correct shape, i.e. the first and fifth pads had pulse heights which were smaller than the second and fourth pads, respectively. This also discarded data where two tracks passed through the pad chamber within two pads of each other. The cut on the number of pads above threshold was two and the threshold was set to 3σ above zero, calculated from the pedestal for each pad. The amount of data that failed each of these cuts (when the cuts were applied independently) is shown in Table 2. The total fraction of all the raw data that was kept after the above cuts was 17%. The efficiency of finding a cluster with at least two hits above threshold and no saturation was about 90% depending on the operating voltage as seen from Table 2.

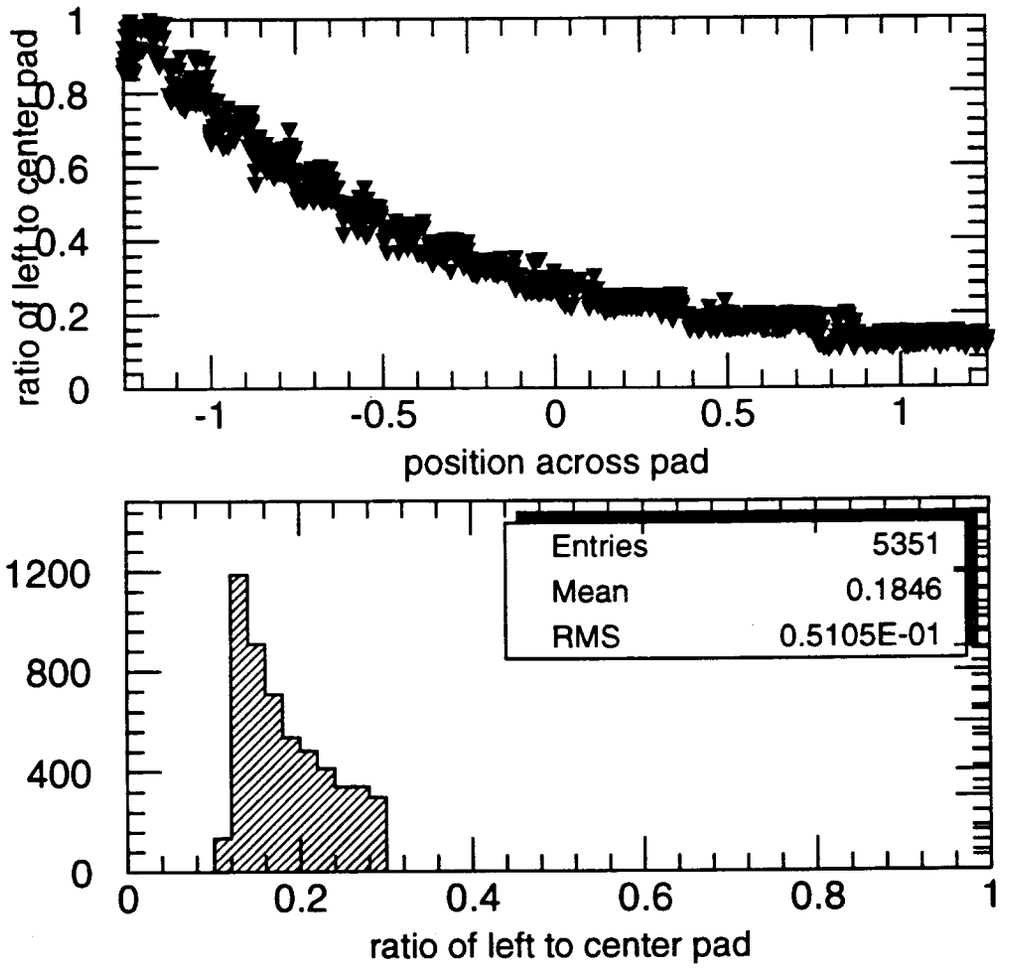

Figure 23: The ratio of the left to the center pad, $\mathcal{M}_d$, as a function of the position across the center pad (top), and its projection (bottom).

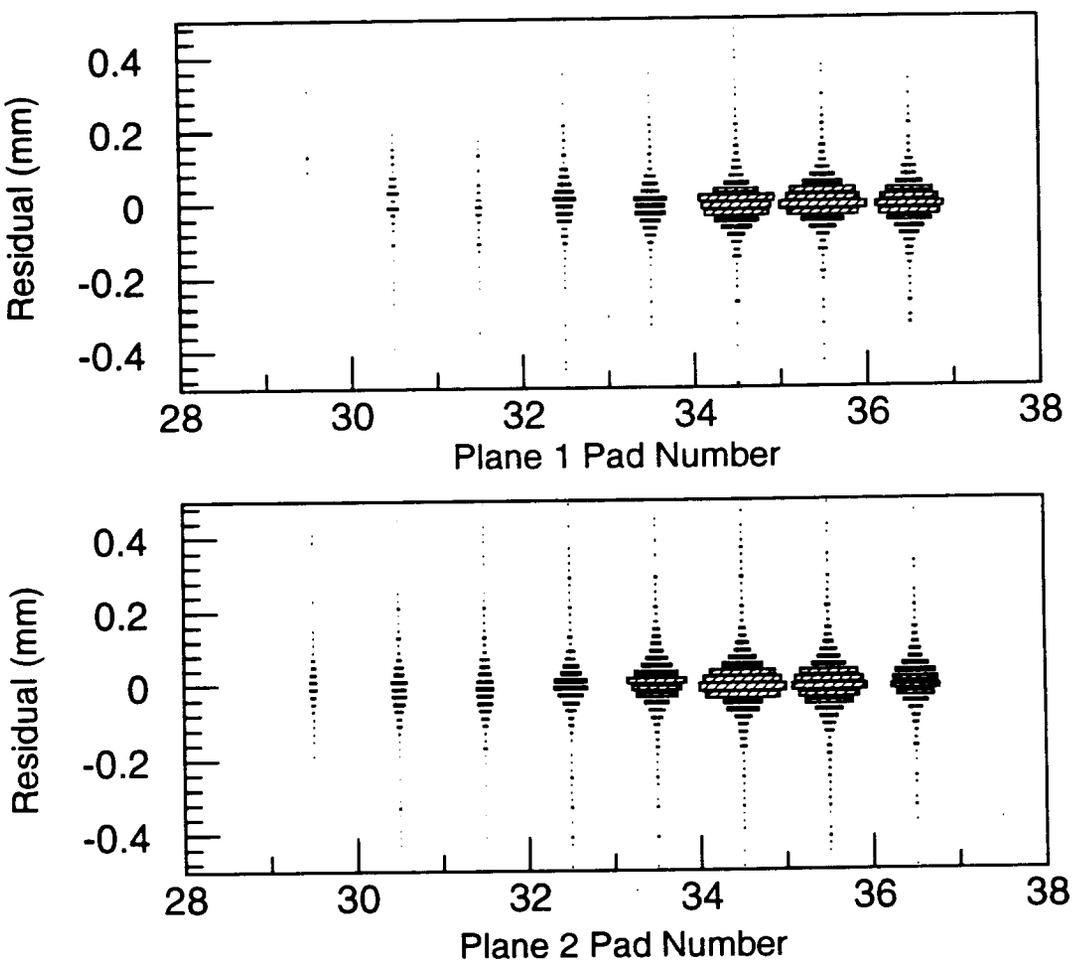

Figure 24: The resolution of IPC plane 1 and plane 2 versus pad number after the software calibration procedure.

Data Cut	V = 2650	V = 2675	V1=2550,V2 = 2725	V = 2750
IPC 1 Saturated	0.045	0.062	0.016	0.162
IPC 2 Saturated	0.055	0.073	0.136	0.198
less than 1 y Si hit	0.135	0.136	0.109	0.114
less than 1 x1 Si hit	0.096	0.100	0.079	0.084
less than 1 x2 Si hit	0.073	0.105	0.079	0.082
less than 1 x3 Si hit	0.340	0.311	0.145	0.073
less than 1 IPC 1 hit	0.104	0.083	0.229	0.156
less than 1 IPC 2 hit	0.065	0.079	0.130	0.191
more than 1 y Si hit	0.213	0.141	0.280	0.224
more than 1 IPC 1 hit	0.050	0.029	0.039	0.045
more than 1 IPC 2 hit	0.043	0.024	0.052	0.041
no Si track	0.028	0.017	0.063	0.043
Total kept	0.157	0.199	0.203	0.198

Table 2: The fraction of data that failed various data cuts, as well as the total fraction of events that were kept for four separate voltage settings of the IPC's.

4.2 Pad Resolution Measurement

4.2.1 Resolution in x

The resolution in the x direction was measured separately for each IPC plane. The position that was measured in each of the IPC planes was in the direction transverse to the pads. Remember, the pads were at an angle of 50 mRad with respect to the y axis. This measurement was then transformed into a value of x using the y measurement provided by the silicon in order to be able to measure the resolution of each plane separately. The vertical beam divergence, which was estimated to be about 2 mRad from the ray tracing program TURTLE and is shown in Figure 25 [8] contributed an effective uncertainty of 20 μm in the x measurement from the information about the y position measured in the first silicon layer. The difference between this x measurement and that predicted by the silicon telescope was then studied as a function of the pad number, the distance between the chamber hit and the center of the peak pad hit, the x distance across the chamber, the y distance across the chamber, and the value of the peak pad pulse height.

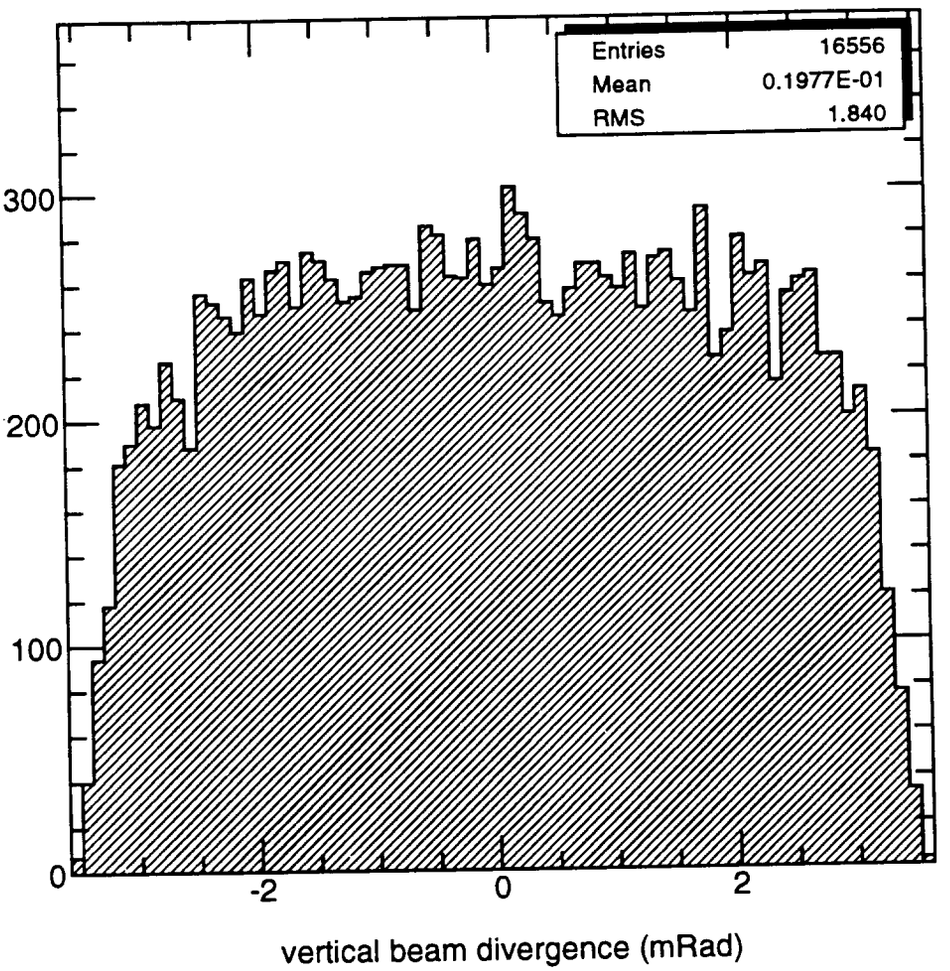

Figure 25: The vertical beam divergence as calculated from the ray tracing program TURTLE.

Resolution data were collected at five separate detector voltage settings and the results are shown in Table 3 and in Table 4 where the vertical beam divergence has been corrected for. The resolution measurements tend to be better for the larger data sets and this can be attributed to the fact that there were more events available here for calibration. Although there was very little change in the resolution from V = 2650 to V = 2750, a larger number of events had saturated pads. The one exception is the data collected for plane one at a detector voltage of 2550 V, which does show a degredation in the resolution to 65 μm because of poorer signal to noise.

Plane	V = 2550	V = 2650	V = 2675	V = 2725	V = 2750
IPC 1 sigma	57	50	51	-	54
IPC 1 mean	1.0	−9.0	1.0	-	0.7
IPC 2 sigma	-	57	49	49	56
IPC 2 mean	-	−3.0	−2.0	−2.0	7.3
No Events	3809,0	1334,1805	2840,3809	0,5649	986,1335

Table 3: The means and sigmas of the residual distributions for plane 1 and plane 2 at the different detector voltage settings. The divergence of the beam in the yz plane is included in the residuals. Also listed are the number of events that were used to determine the resolutions for each voltage setting and each detector plane.

Plane	V = 2550	V = 2650	V = 2675	V = 2725	V = 2750
IPC 1 sigma	54	47	48	-	51
IPC 1 mean	1.0	−9.0	1.0	-	0.7
IPC 2 sigma	-	54	46	46	53
IPC 2 mean	-	−3.0	−2.0	−2.0	7.3
No Events	3809,0	1334,1805	2840,3809	0,5649	986,1335

Table 4: The means and sigmas of the residual distributions for plane 1 and plane 2 at the different detector voltage settings with the error that is caused by the divergence of the beam removed. Also listed are the number of events that were used to determine the resolutions for each voltage setting and each detector plane.

Since the statistics are best at 2675 V for plane one and 2725 V for plane 2, the results are presented for these data sets. The means and sigmas of the residuals versus pad number are shown in Figure 26 for plane 1 and in Figure 27 for plane 2. In these plots each pad was required to have at least 100 entries to enable a Gaussian fit to be carried out on the residual distribution. Furthermore, only clusters with three pads above threshold were used in the cluster finding algorithm. What is apparent from these plots is that the *intrinsic* resolution of the IPCs is around 45 μm (this is just a measure of the width of the residual for the pad when it is the center pad in the cluster) but that the variation around zero of the mean of the residuals for each pad has a sigma on the order of 10 μm which will limit the overall resolution achievable. This is a symptom of the limits of the calibration procedure.

The distributions for all pads in plane 1 at 2675 V and plane 2 at 2725 V can be seen in Figure 28. The widths of these distributions must be corrected for 12 μm projection error and 20 μm from the vertical beam divergence. The resulting resolutions are 45 μm and 46 μm for planes 1 and 2 respectively. The mean of the residual distribution is close to zero across the area that was covered by the electronics, as shown in Figure 29, where the residual versus x and y distance across the chamber is shown for both planes, except for the last few bins which correspond to the end pad which could not be calibrated with the software procedure. The resolution is also found to be independent of the distance the hit is from the center of the peak pad as shown in Figure 30 and Figure 31. This implies that the Mathieson function solved for three pads works equally well for hits where the peak of the charge distribution falls almost between two pads as it does when the peak is in the middle of the pad. Finally, the resolution as a function of the total pulse height of the cluster is presented in Figure 32 and Figure 33. Here there is a dependence of the resolution on the total pulse height. Binning the data as a function of pulse height is similar to looking at the resolution as a function of gain. Unfortunately, the statistics at the high and low ends of the pulse height spectra are poor. The degredation at small pulse heights is likely to be a result of poor signal to noise. A possible explanation for the degredation at the high end is that the large pulse height is due to a delta ray close by which will degrade the resolution.

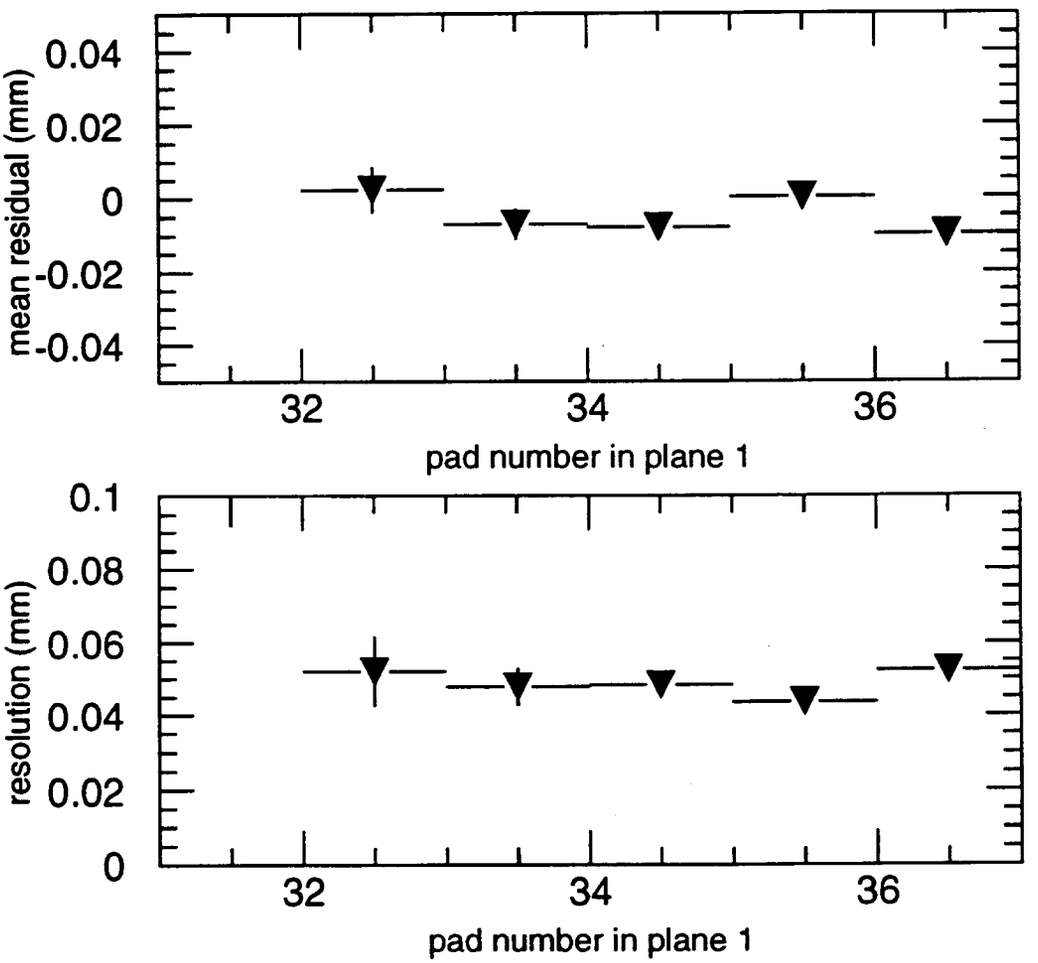

Figure 26: The means and sigmas from a Gaussian fit to the residuals of each pad for plane 1 at 2675 V.

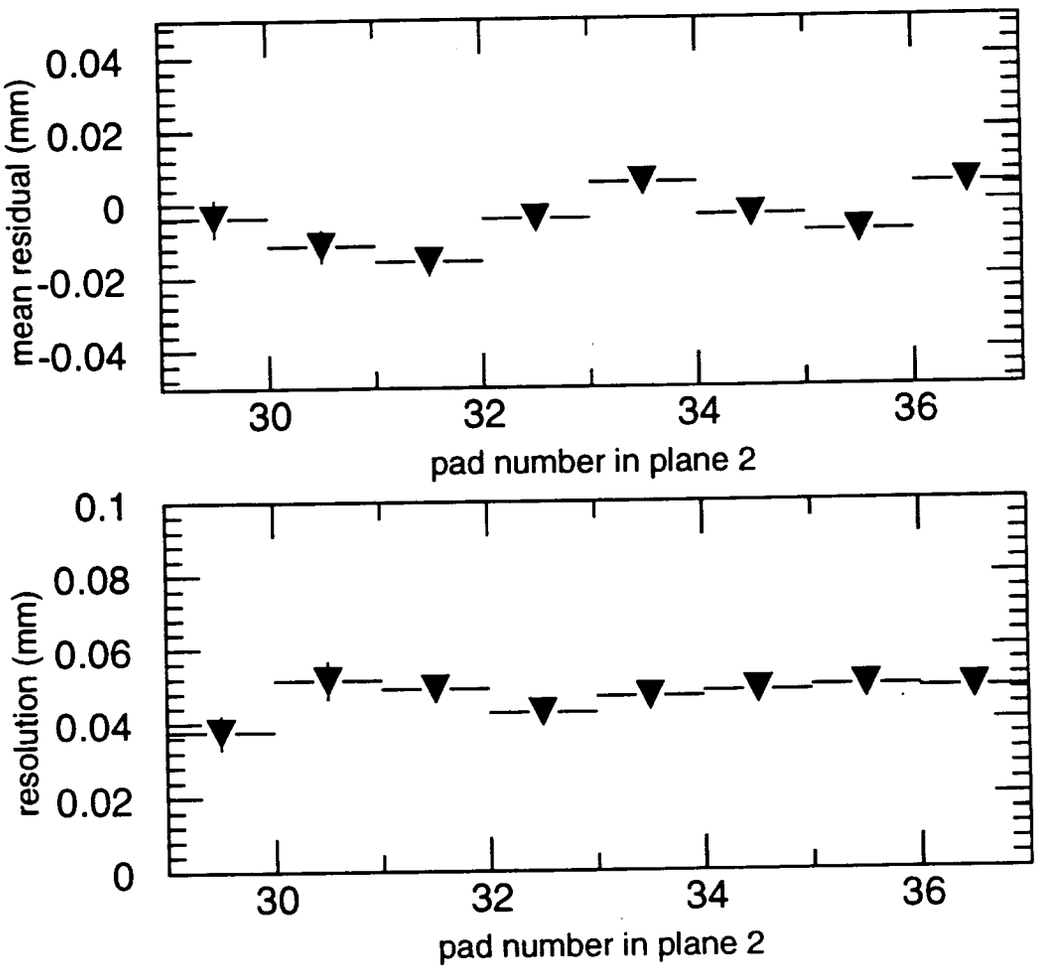

Figure 27: The means and sigmas from a Gaussian fit to the residuals of each pad for plane 2 at 2725 V.

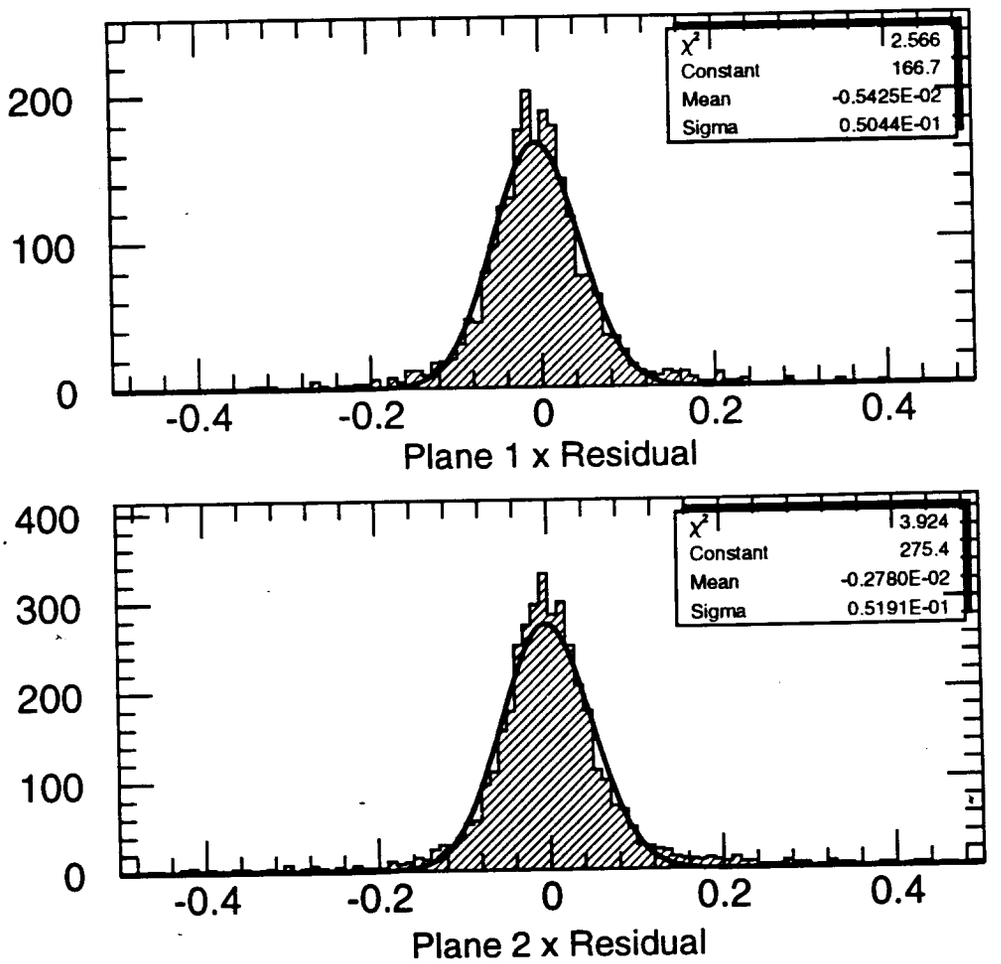

Figure 28: The residual distributions for the highest statistics runs for each IPC plane with a gaussian fit to the distribution. This must be corrected for the 12 μm projection error and 20 μm vertical beam divergence uncertainty. The resulting resolutions are 45 μm and 46 μm for planes 1 and 2 respectively.

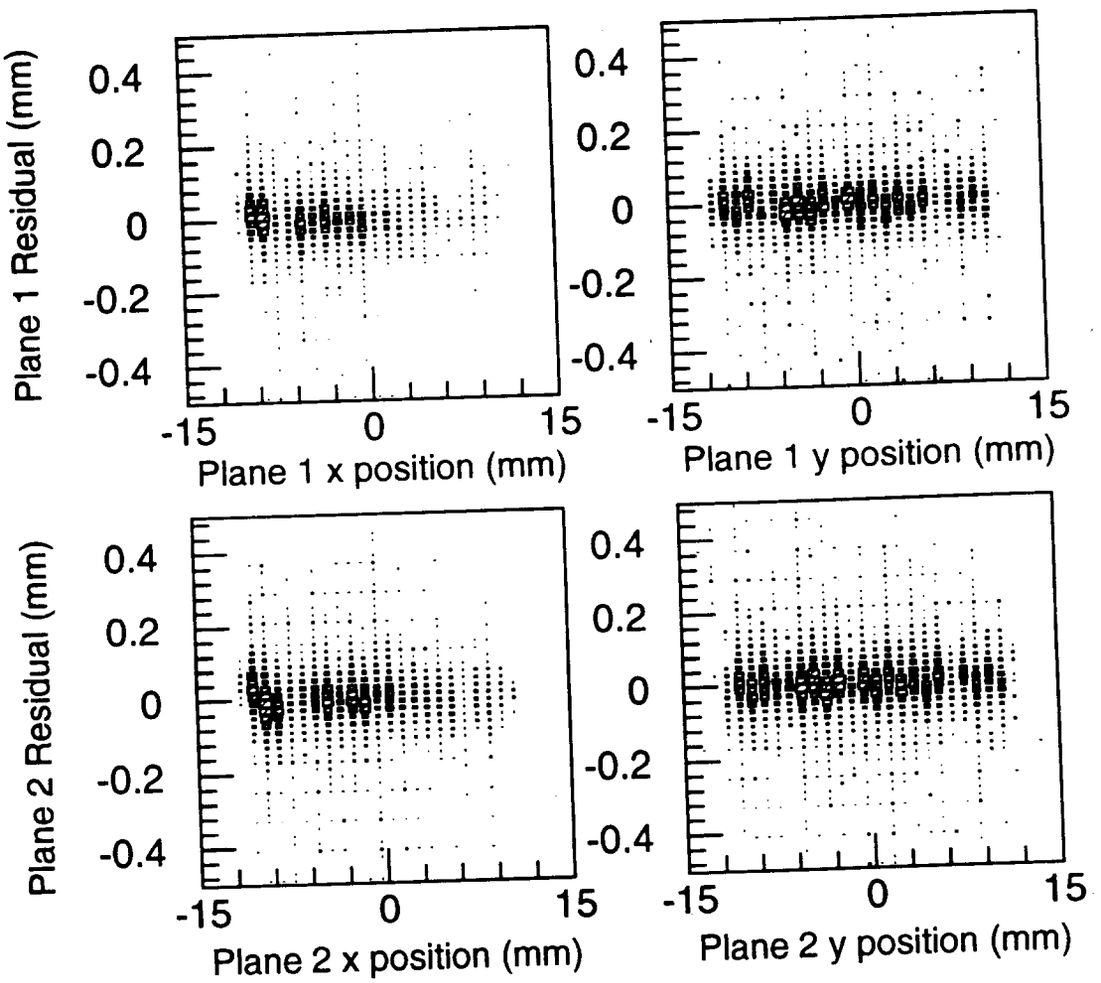

Figure 29: The residuals of each IPC plane versus the x position in the chamber and vs. the y position (uncorrected).

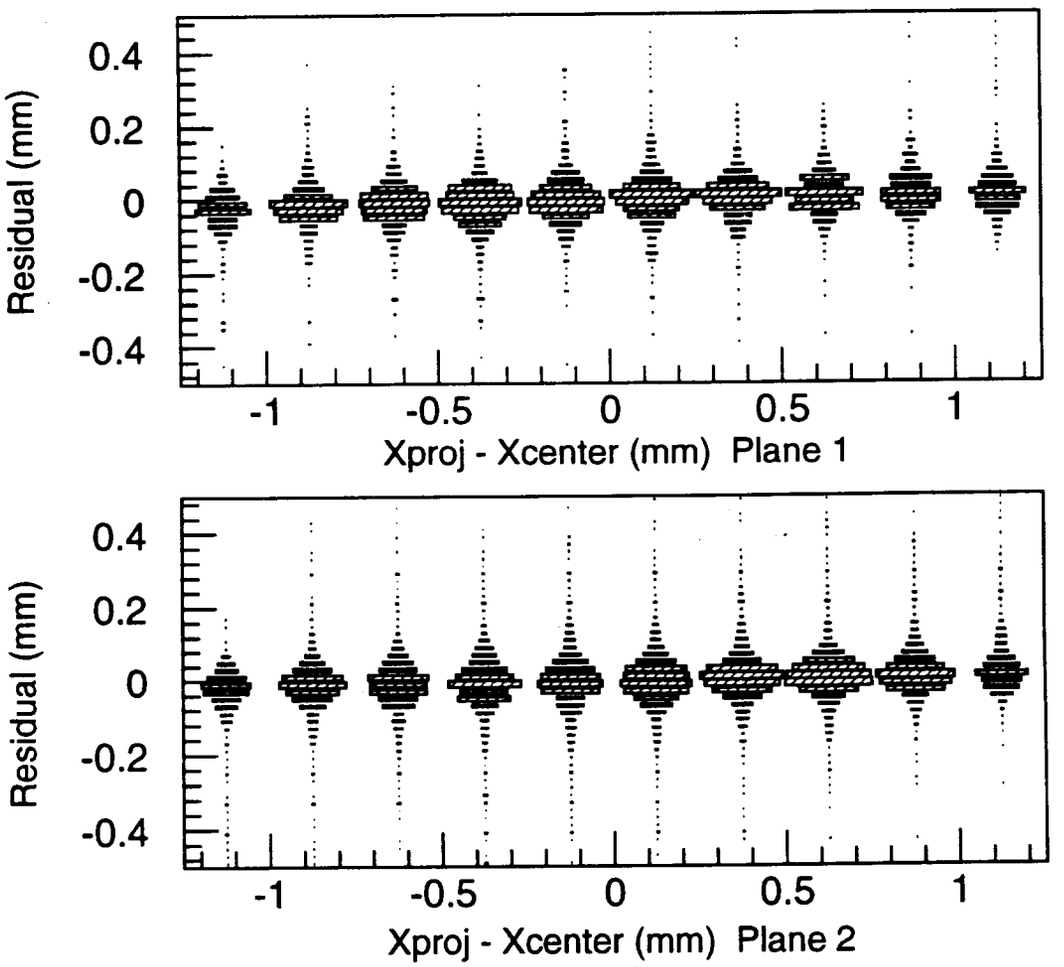

Figure 30: The residuals of each IPC plane versus the distance of the projected hit from the center of the peak pad (uncorrected).

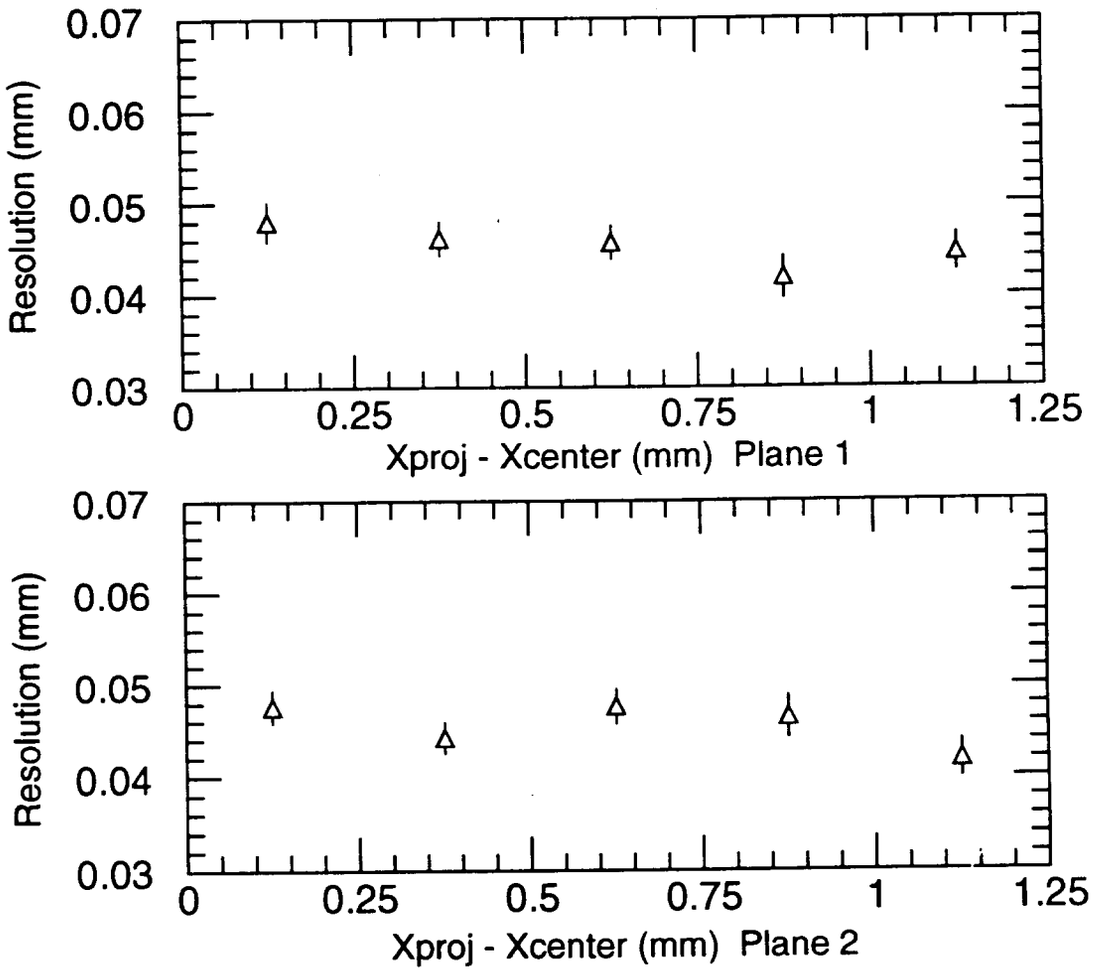

Figure 31: The resolution of each IPC plane versus the distance of the projected hit from the center of the peak pad. These data are corrected for the projection error and the vertical beam divergence.

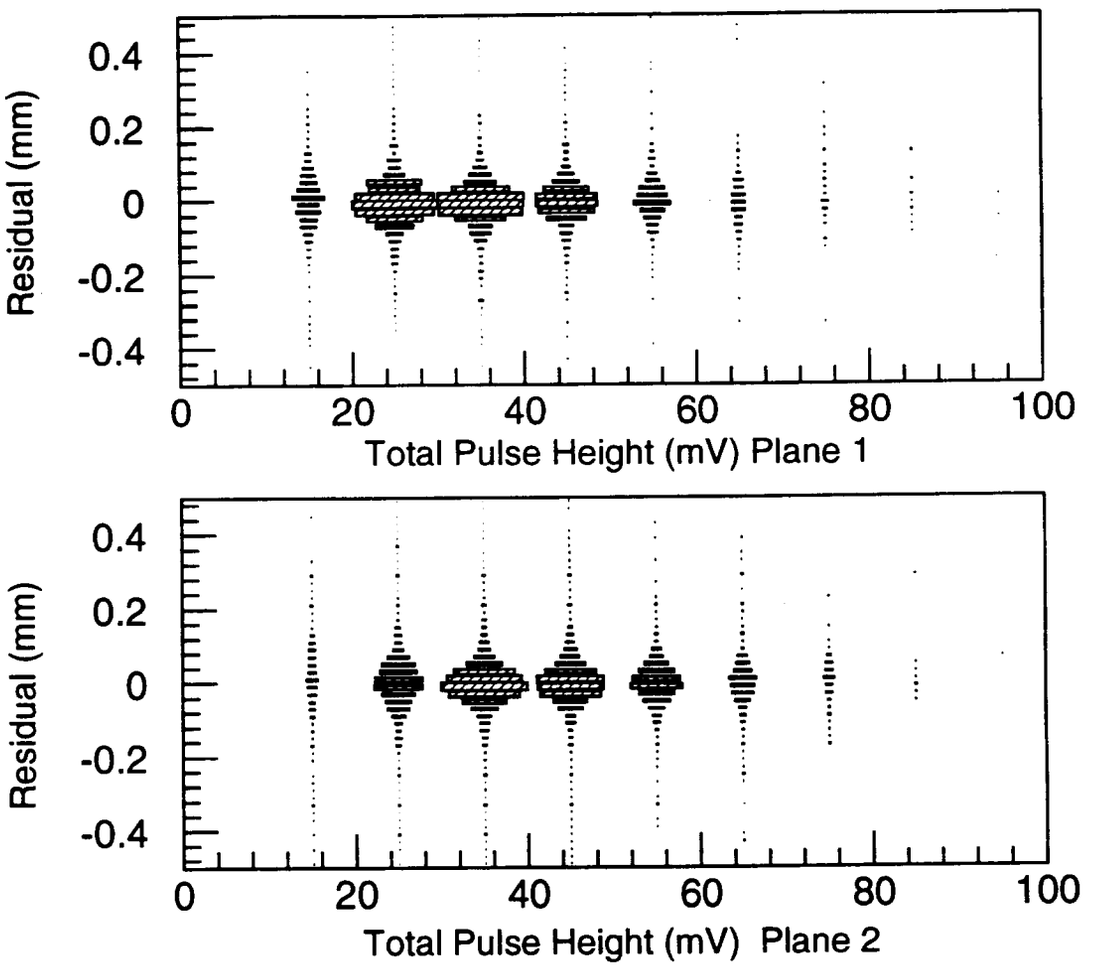

Figure 32: The residuals of each IPC plane versus the total pulse height in the cluster (uncorrected).

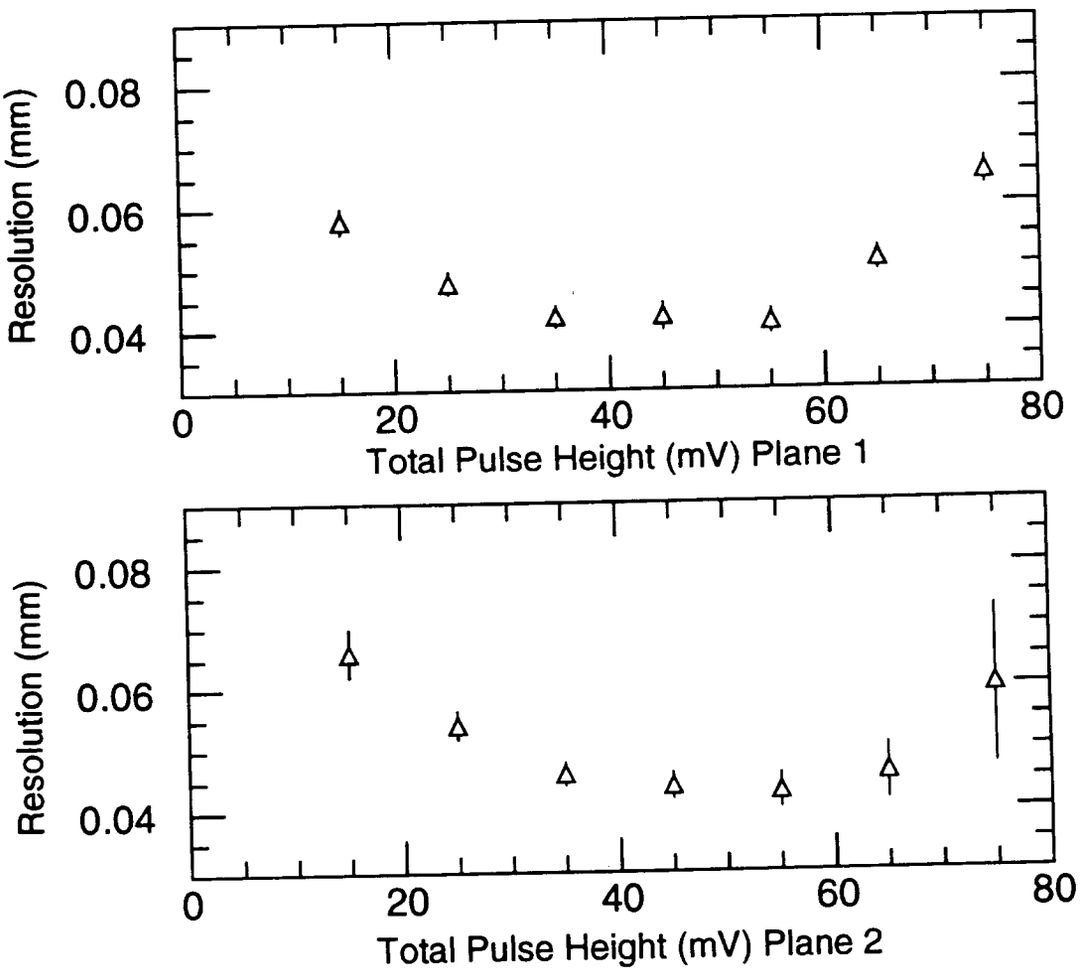

Figure 33: The resolution of each IPC plane versus the total pulse height in the cluster These data are corrected for the projection error and the vertical beam divergence.

4.2.2 Resolution in y

For events with hits in both IPC planes, the y resolution was calculated by finding the intersection of the two lines which pass through the two measured clusters and have the slopes of the stereo angles of the two planes. The y resolution obtained from the data collected at 2675 V (which had the best overall calibration data) is shown in Figure 34, where the difference between the y measurement and the y value predicted by the silicon is shown. After correction for the vertical beam divergence, the resolution obtained is approximately 680 μm.

4.2.3 Resolution Using Two Pads

The Mathieson function can also be solved using any two out of the three pads if K_3 is fixed to the value predicted by the geometry. This was attempted separately for the two side pads and the center and side pad. This is of interest if a single electronics channel is not functioning or a single pad is grounded.

Using just the two side pads, the resolutions achieved are 61 μm in plane 1 and 62 μm in plane 2 after correction for the vertical beam divergence as shown in Figure 36. There was no dependence of this resolution on pad number and there were no substantial offsets in the residual distributions. However, the resolution does degrade when the ratio of the two pulse heights becomes small. This can be seen in Figure 35 where the resolution is shown vs. the natural log of the ratio of the left pulse height to the right pulse height. As the pulse on the left pad becomes small, the measured x position moves to the right of the actual hit, and as the pulse height on the right pad becomes small, the measured position moves to the left of the actual hit.

Using just the middle pad of the hit distribution and a pad to one side, the resolution that was obtained is shown in Figure 37 versus the ratio of the peak pad pulse height to the side pad pulse height. The dependence of the resolution on the pulse height ratio is similar to the dependence that was seen when the two side pads were solved for the Mathieson function: as the side pad pulse height becomes small, the measured position in the chamber moves away from the true hit and toward the peak pad that has the larger pulse height. The resolutions that are obtained when the distribution across the entire pulse height range is fit to a gaussian is 81 μm in plane 1, and 78 μm in plane 2 (77 μm and 74 μm when corrected for vertical beam divergence and projection error) as shown in Figure 38. Comparison of this result with the former case indicates that the ratio of the two side pads is more important than the magnitude of the middle pad signal.

It is suspected that the systematic shifts in the residuals at the edges of Figures 35 and 36 are due to insufficient calibration for small pad pulse heights. These same amplifier/ADC combinations had been shown previously to have non-linearities at the low end of their range, and unfortunately, our calibration procedures for the current tests did not take this into account.

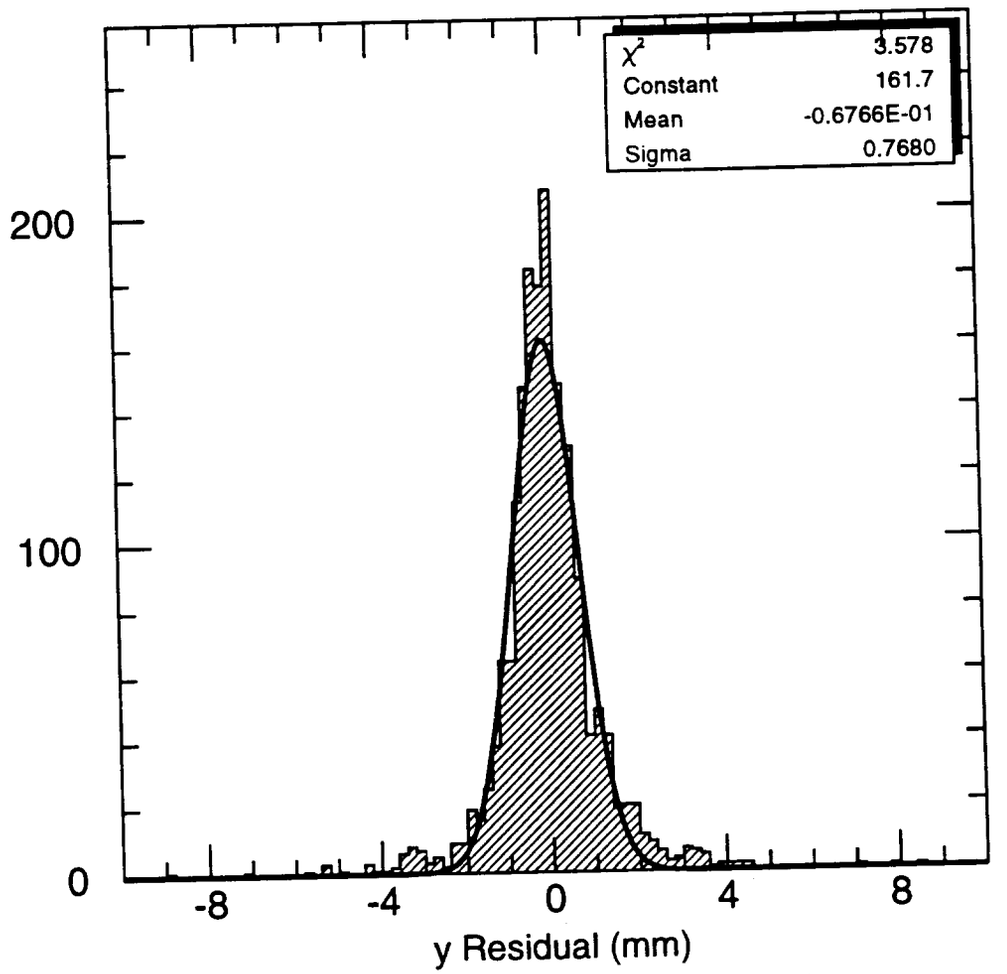

Figure 34: The residual distribution in y of the combined IPC planes for detector voltage = 2675 V. After correction for the vertical beam divergence, the resolution obtained is approximately 680 μm.

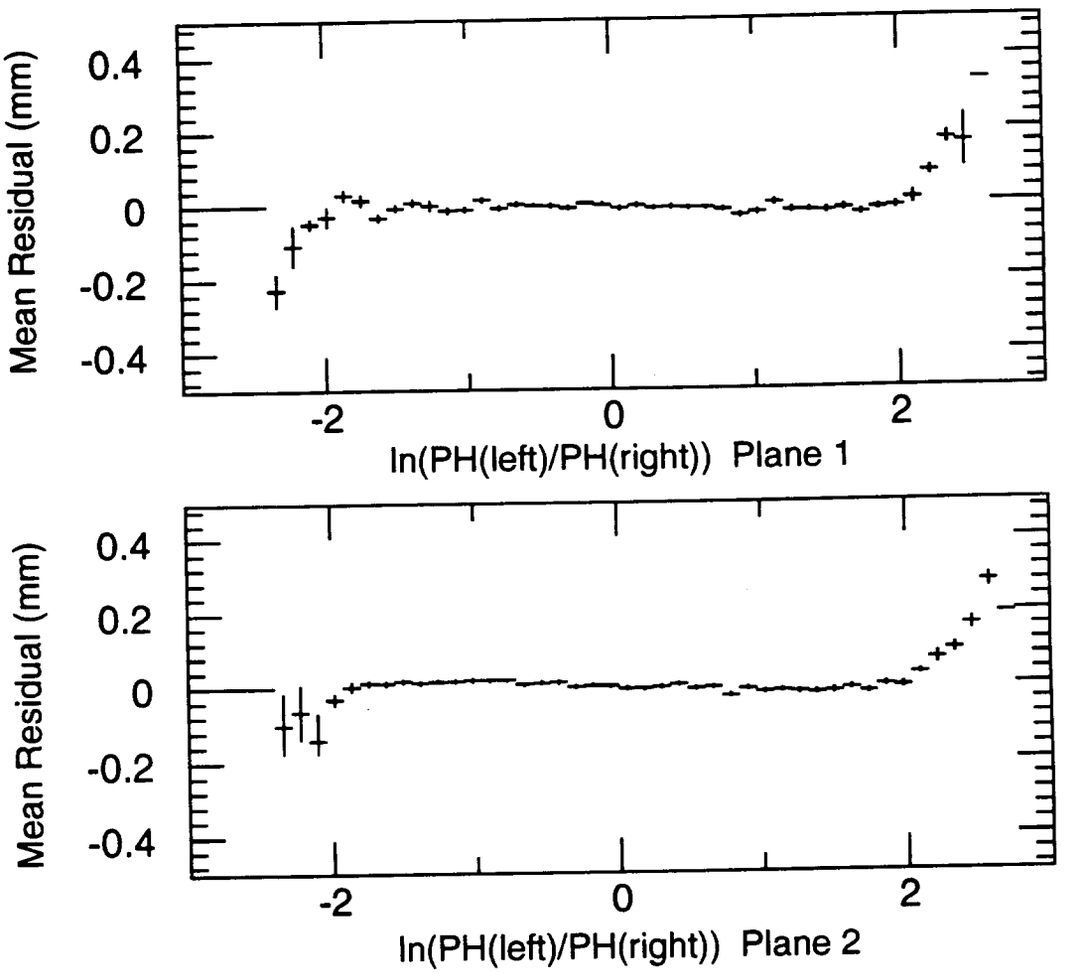

Figure 35: The mean residual for a two pad fit of each IPC plane versus the log of the ratio of the pulse height in the left pad to the pulse height in the right pad.

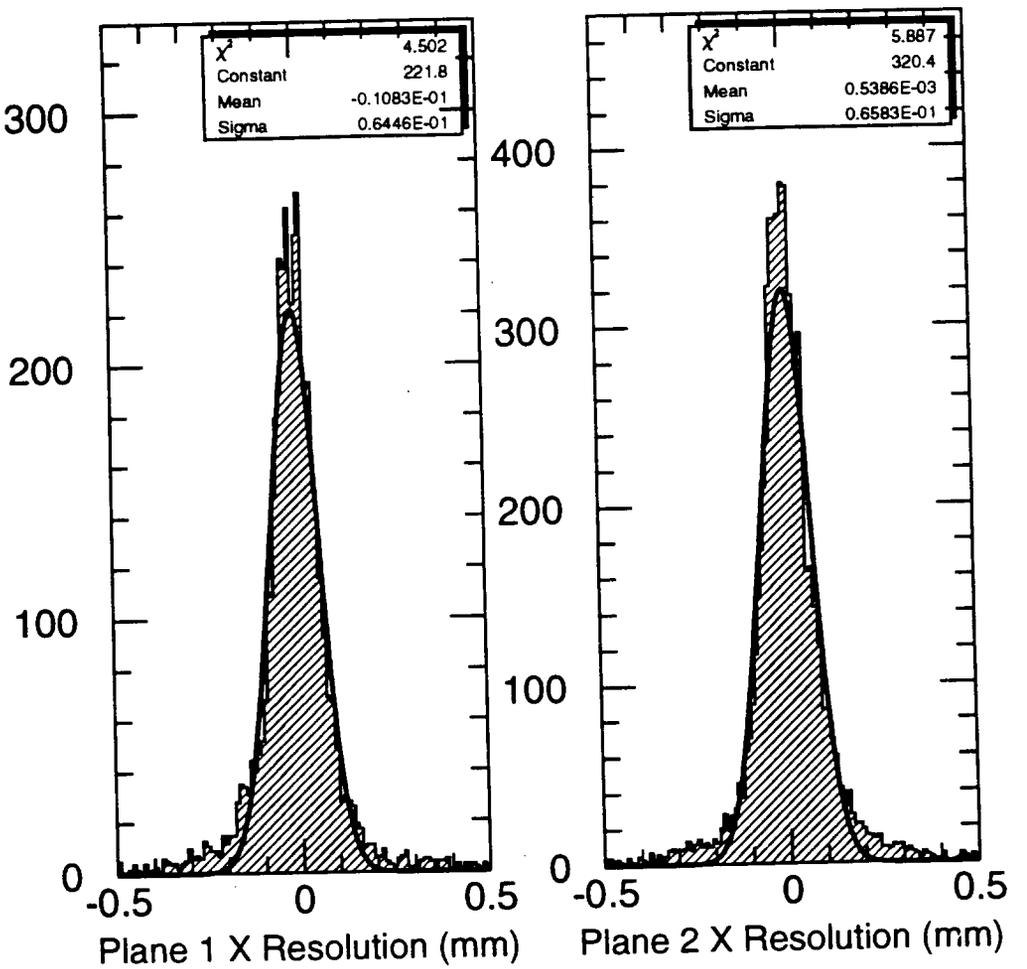

Figure 36: The resolution for a two pad fit (when the two pads are the side pads of each IPC plane (uncorrected).

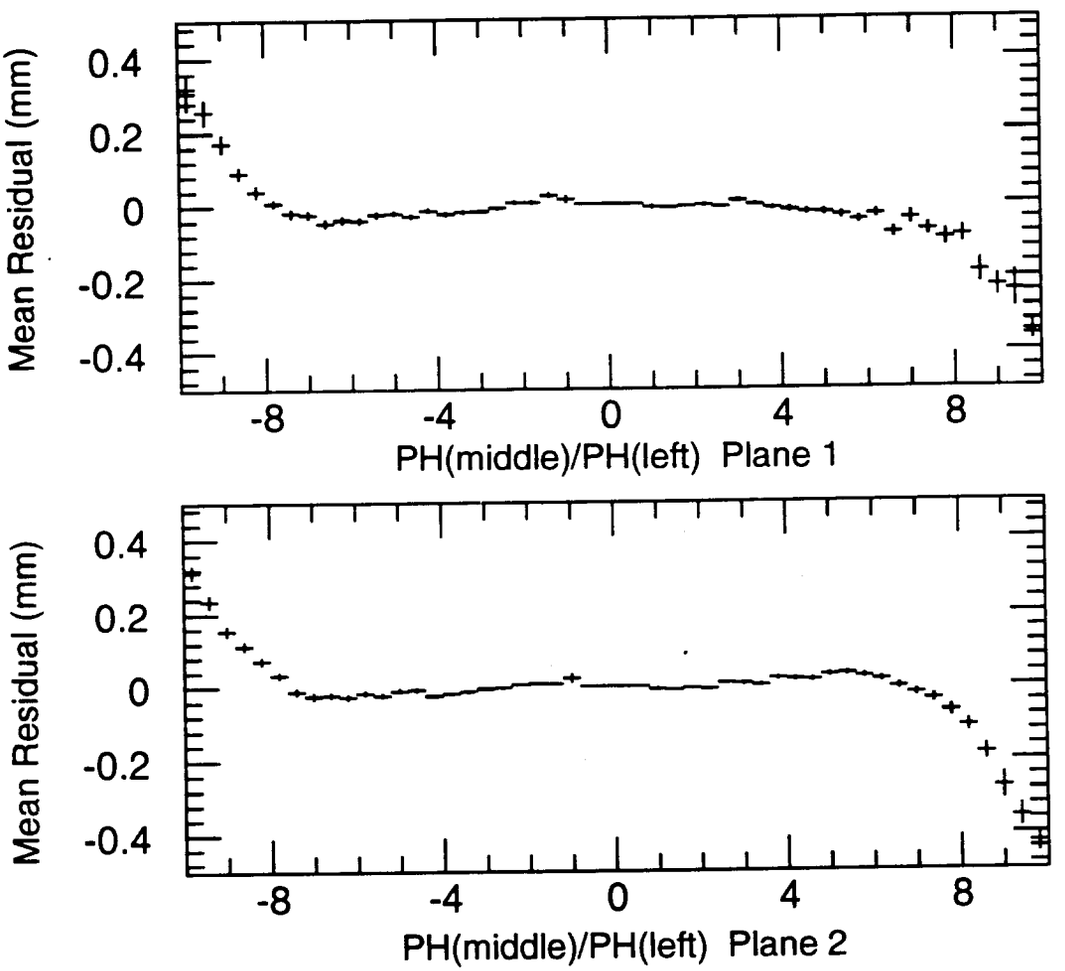

Figure 37: The mean of the residual for a two pad fit (when the two pads are the middle pad and one of the side pads) of each IPC plane versus the ratio of the pulse height in the middle pad to the pulse height in the side pad.

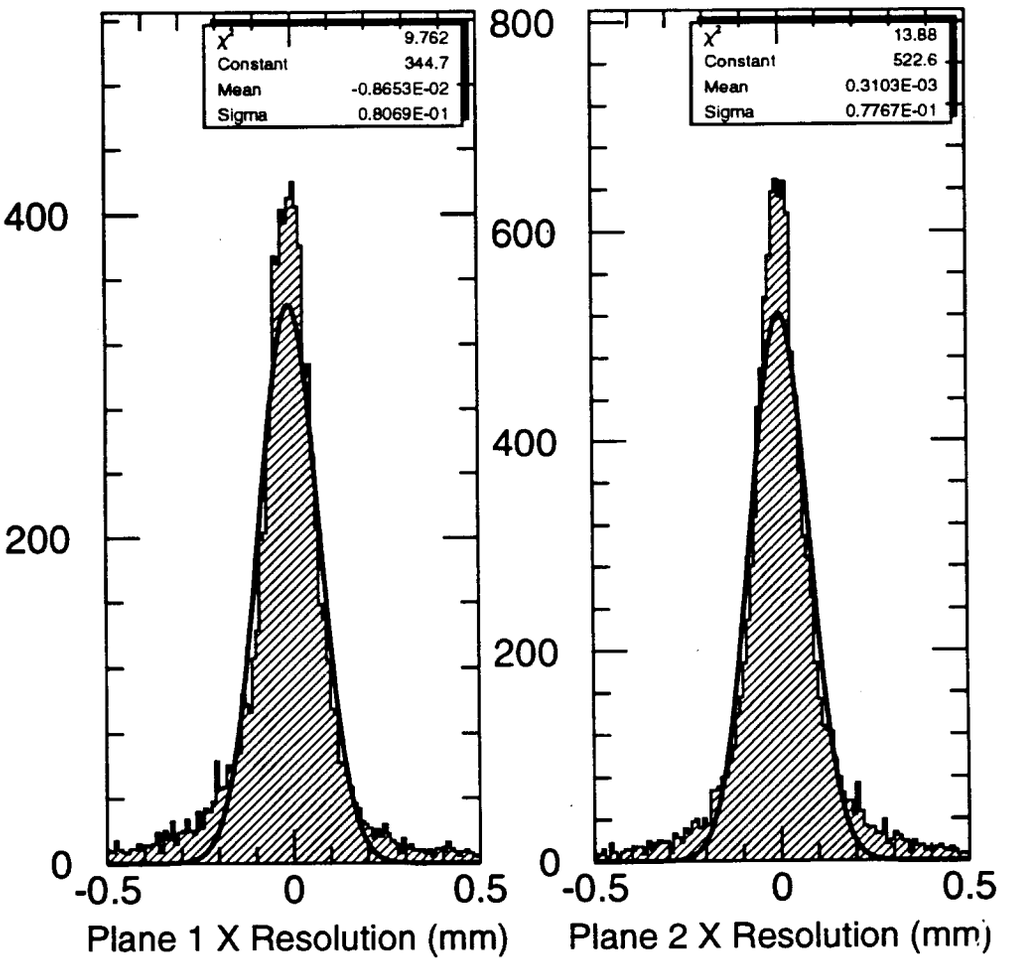

Figure 38: The resolution for a two pad fit (when the two pads are the middle pad and one of the side pads) of each IPC plane (uncorrected).

4.2.4 Untreated Systematics

As noted previously, the environment of the BNL test beam was extremely noisy. Vacuum pumps caused the floor to vibrate and also the frame holding the chamber. It was not possible to measure the magnitude of this vibration in the x direction at the pad layer, but on the frame the vibrations were large enough to be felt by hand. In the absence of any concrete measurement, this added systematic effect has been ignored although its contribution is present in the resolution measurement.

5 Conclusion

A resolution of 45 μm has been achieved in the prototype GEM tracker barrel IPC. Effects of pad to pad variations have been effectively reduced to the 2% level with a calibration procedure which makes use of the data. However, this calibration procedure will probably not be workable in the GEM environment, and so it is of crucial importance that all systematic effects be understood to 1%. This has not been demonstrated. The resolution has been studied using two and three pads in the cluster finding algorithm and it has been established that the effect of dead channels is not necessarily catastrophic.

6 Acknowledgments

We would like to thank Dave Dayton and the staff at the Brookhaven National laboratory AGS facility for their first class assistance during the test beam run. Also we would like to thank Leonard Archer for his help in preparing this document.

References

[1] Micron Semiconductor Inc., 126 Baywood Ave, Longwood, Florida 32750.

[2] CDF svx-D chip.

[3] NOMEX is a trade mark of Du Pont.

[4] EPON is a trade mark of Shell Oil Company.

[5] Oxy-Bond 119T2 is manufactured by Resin Technology. This epoxy has a similar specification to HYSOL, widely used in the aerospace industry.

[6] Botlo et al., GEM TN-93-369

[7]
- E. Mathieson, NIM A270 (1988) 602–603
- E. Mathieson and J.S. Gordon, NIM 227 (1984) 277–282

[8] Kenneth Barish, Yale University representing the E864 collaboration.